

## Boundary-corrected four-body continuum-intermediate-state method: Single-electron capture from heliumlike atomic systems by fast nuclei

Ivan Mančev,<sup>1</sup> Nenad Milojević,<sup>1</sup> and Dževad Belkić<sup>2</sup>

<sup>1</sup>*Department of Physics, Faculty of Sciences and Mathematics, University of Niš, P.O. Box 224, 18000 Niš, Serbia*

<sup>2</sup>*Karolinska Institute, Department of Oncology-Pathology, P.O. Box 260, S-171 76 Stockholm, Sweden*

(Received 5 February 2015; revised manuscript received 1 May 2015; published 5 June 2015)

Single charge exchange in collisions between bare projectiles and heliumlike atomic systems at intermediate and high incident energies is examined by using the four-body formalism of the first- and second-order theories. The main purpose of the present study is to investigate the relative importance of the intermediate ionization continua of the captured electron compared to the usual direct path of the single electron transfer from a target to a projectile. In order to achieve this goal, comprehensive comparisons are made between the four-body boundary-corrected continuum-intermediate-states (BCIS-4B) method and the four-body boundary-corrected first Born (CB1-4B) method. The perturbation potential is the same in the CB1-4B and BCIS-4B methods. Both methods satisfy the correct boundary conditions in the entrance and exit channels. However, unlike the CB1-4B method, the second-order BCIS-4B method takes into account the electronic Coulomb continuum-intermediate states in either the entrance or the exit channel depending on whether the post or the prior version of the transition amplitude is used. Hence, by comparing the results from these two theories, the relative importance of the intermediate ionization electronic continua can be assessed within the four-body formalism of scattering theory. The BCIS-4B method predicts the usual second-order effect through double scattering of the captured electron on two nuclei as a quantum-mechanical counterpart of the Thomas classical two-step, billiard-type collision. The physical mechanism for this effect in the BCIS-4B method is also comprised of two steps such that ionization occurs first. This is followed by capture of the electron by the projectile with both processes taking place on the energy shell. Moreover, the role of the second, noncaptured electron in a heliumlike target is revisited. To this end, the BCIS-4B method describes the effect of capture of one electron by the interaction of the projectile nucleus with the other electron via the static electron-electron correlations in the target. This effect yields a novelty seen as the second Thomas peak. As an illustration, detailed computations were carried out involving both the differential and total cross sections for one-electron capture in the  $p - \text{He}$  collisions at intermediate and high impact energies. The results obtained in the BCIS-4B method are compared with those from the CB1-4B method and with the available experimental data. The overall usefulness of the BCIS-4B method is assessed in predicting experimental data for four-body single charge exchange both qualitatively (shapes of cross sections) and quantitatively (numerical values from measurements).

DOI: [10.1103/PhysRevA.91.062705](https://doi.org/10.1103/PhysRevA.91.062705)

PACS number(s): 34.70.+e, 82.30.Fi

### I. INTRODUCTION

Fast ion-atom collisions have attracted a great deal of attention by both theoretical and experimental investigations over many decades. There are several reasons for this. First, high-energy collisions are of paramount practical importance across interdisciplinary fields ranging from astrophysics to medicine [1–8]. Among these collisions, the central place was and still is within charge exchange and ionization both for one- and two-electron processes. Second, the emergence of more detailed and more accurate experimental data has prompted the development of new theoretical methods aimed at better understanding the fundamental aspects of few-body dynamics.

In the past, an accurate technique known as the cold target-recoil ion momentum spectroscopy (COLTRIMS) has been developed for experimental study of atomic collision systems. The COLTRIMS technique has proven to be a powerful tool for revealing the details of the interactive dynamics of atomic collisions [9]. For example, within the past decade a number of experimental measurements [10–18] of differential cross sections for single charge exchange in  $p - \text{He}$  collision via the COLTRIMS technique have spurred renewed interest in theoretical calculations by means of a variety of methods [19–30].

The present work is aimed at a thorough theoretical investigation of single electron capture from heliumlike atomic

systems by bare projectiles using the four-body boundary-corrected continuum-intermediate-state (BCIS-4B) method. This approximation is an adaptation of the same method introduced by Belkić [31] in 1993 for double electron capture in collisions of fast nuclei with heliumlike atomic systems. The forerunner of this formalism is the three-body continuum-intermediate state (CIS-3B) method for charge exchange between bare nuclei and hydrogenlike atomic systems proposed by Belkić [32] in 1977. Both the CIS-3B method and its four-body counterpart, the CIS-4B method, satisfy the correct boundary conditions only in one channel (entrance or exit, depending on whether the post or the prior form of the transition amplitude is used). For example, in the prior version, the CIS-4B and BCIS-4B methods for single charge exchange between completely stripped nuclei and heliumlike targets have the identical description of the exit channel with the electronic Coulomb wave function centered on the screened target nuclear charge. The difference is in the asymptotic wave function and the perturbation potential in the entrance channel, where the undistorted initial state is multiplied by the two unequal logarithmic Coulomb phases due to the nonscreened and screened (via two electrons) internuclear potential in the prior versions of the CIS-4B and BCIS-4B method, respectively.

Collisional processes in which two nuclei and two electrons take part represent pure four-body problems. Such a simple four-body system provides substantial information for a better comprehension of the fundamental dynamics in more involved few-body collision systems. A large number of theoretical studies have been performed using different four-body methods for studying various one- and two-electron transitions in scattering of completely stripped projectiles on heliumlike atomic systems or in collisions between two hydrogenlike atoms or ions, as recently reviewed in Refs. [1–8].

It is well known that ion-atom collisions involve long-range Coulomb potentials that persist even when the scattering particles are located at infinite separations from each other. Such an effect causes Coulombic phase distortions of the unperturbed channel states. This, in turn, modifies the associated perturbation potentials. The concept of the correct Coulomb boundary conditions is equivalent to the concept of asymptotic convergence [1,2,5,6,33,34]. This is because both concepts share the same physical basis which aims at distinguishing the asymptotically free states from those stemming from the interactive dynamics. Such a disentangling is a key to unequivocal predictions for which it is essential to infer what actually happened during the collisional event by using the final state of the system. At first, this seems to be untenable for Coulombic collisions. Namely, an asymptotically present Coulombic potential would continue to distort the channel states that, therefore, cannot ever become free. This difficulty is circumvented by way of asymptotic convergence, i.e., the correct boundary conditions. Such an obstacle is far from being of a formal nature. Quite the contrary, without having attained the asymptotically free state of the collision system, the Møller wave operator would not exist, which means that the scattering or the  $S$  operator and the related cross sections would be void of any physical meaning.

The asymptotic convergence problem [34] is formally solved in such a way that the operator-valued Coulomb phase is subtracted from the total Hamiltonian to produce a Coulomb modified Møller wave operator which is well defined in the sense of securing the existence of the asymptotically free states of the entire system. Although such a modification of the Hamiltonian is formally adequate, it is, nevertheless, difficult to implement in practice because of the complicated form of the time evolution operator containing an exponential function of the square root of the kinetic-energy operator.

The correct boundary condition problem in the coordinate representation [1] comes to the rescue, since it consists of subtracting the Coulombic *scalar* phases from the channel states rather than having to deal with the associated *operator*-valued phases encountered in the asymptotic convergence problem [34]. However, and most importantly, this latter scalar phase modification [1] must simultaneously be followed by the associated alteration (also in the scalar form) of the perturbation potential. So here too (i.e., within the concept of the correct boundary conditions [1]) there are modifications of operators, albeit in a much less complicated form than in the Dollard evolution operator [34]. It is because of this simultaneous circumstance (both the phase of the wave function and the perturbation potential ought to be consistently modified) that it must always be born in mind that the correct boundary conditions consist of establishing the proper

asymptotic behaviors of the scattering wave functions *and* the consistently devised perturbation potentials. This is also evident from the fact that the perturbation potential can alternatively be defined as the residual potential left after the application of the operator  $H - E$  on the ansatz scattering state  $\chi$  of the selected model. Here  $H$  and  $E$  are the total Hamiltonian operator and the total scalar energy of the whole system under investigation. The quantity  $(H - E)\chi$  appears directly in the transition amplitude and, thus, is critical to all the ensuing observables, such as probabilities, cross sections, etc.

The BCIS-4B method is a fully quantum-mechanical four-body formalism and it strictly preserves the correct boundary conditions in both collisional channels. This is a second-order theory which provides a fully adequate description of the fact that, in an intermediate stage of collision, the captured electron moves in a Coulomb field rather than propagating freely according to a plane-wave formalism in the Jackson-Schiff first Born (JSB1-4B) approximation [2,6] with incorrect boundary conditions. The four-body boundary-corrected first Born (CB1-4B) method for single-electron capture [35,36], which also obeys the asymptotic convergence criteria for Coulomb potentials [1,5,34] can be obtained as a further simplification of the BCIS-4B method, if the invoked electron Coulomb wave from the latter method is replaced by its long-range logarithmic phase factor for the relative motion of heavy nuclei and, as such, redefined in terms of the corresponding interaggregate separation  $R$ .

A comparison of the transition amplitudes in the BCIS-4B and CB1-4B methods reveals that they both have the same perturbation potentials. Furthermore, in the case of the prior version, the total scattering wave functions of the BCIS-4B and CB1-4B methods are the same in the entrance channel. The only difference is, however, in the exit channel since the BCIS-4B method employs the electronic Coulomb continuum-intermediate wave function centered on the screened target nuclear charge. Hence, by comparing these two theories, we would learn about the relative importance of these intermediate ionization electronic continua and this is one of the main goals of the present study. Another goal is to critically assess the validity of the BCIS-4B method by comparing the obtained results with the available experimental data, not only for total, but also for differential cross sections at intermediate as well as high impact energies. Especially at high energies, double Thomas scattering processes become very significant and it is important to see how this is predicted by the BCIS-4B method. The differential cross sections give more detailed information and provide a more sensitive and more accurate test for establishing the validity of the theories.

Atomic units will be used throughout unless otherwise stated.

## II. THEORY

### A. Kinematics and dynamics of four-body single charge exchange

We consider single charge exchange between fast heavy atomic nuclei as projectiles and heliumlike targets. The quantum-mechanical nonrelativistic scattering theory will be used throughout without accounting for the spin effects. In

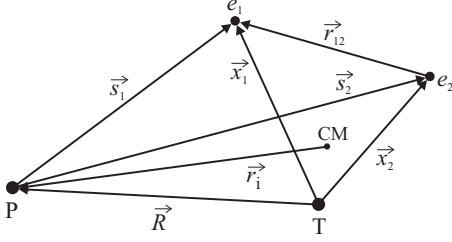


FIG. 1. Coordinate system for the projectile-heliumlike atomic collision.

the spin-independent formalism, the two target electrons can be considered as distinguishable from each other. In such a case, we shall consider that electron  $e_1$  is captured, whereas electron  $e_2$  will remain in the target rest. Since  $e_1$  and  $e_2$  can, in fact, be captured with equal probabilities, the cross section for single-electron capture should be multiplied by 2. This charge exchange process under study is symbolized as follows:

$$Z_P + (Z_T; e_1, e_2)_i \longrightarrow (Z_P, e_1)_{f_1} + (Z_T, e_2)_{f_2}, \quad (1)$$

where  $Z_K$  is the charge of the  $K$ th nucleus, subscript  $j$  ( $= f_1, f_2$ ) is the collective label for the set of the hydrogenlike quantum numbers,  $j = \{n_j, l_j, m_j\}$ , and index  $i$  refers to the quantum numbers of the initial heliumlike state. The parentheses symbolize the bound states in the initial and final channels. Let  $\vec{s}_1$  and  $\vec{s}_2$  ( $\vec{x}_1$  and  $\vec{x}_2$ ) be the position vectors of  $e_1$  and  $e_2$  relative to the nuclear charge of the projectile  $Z_P$  (target  $Z_T$ ). Further, let  $\vec{R}$  denote the position vector of  $Z_P$  with respect to  $Z_T$ , where  $\vec{R} = \vec{x}_1 - \vec{s}_1 = \vec{x}_2 - \vec{s}_2$ . The vector of the distance between the active or captured ( $e_1$ ) and passive or noncaptured ( $e_2$ ) electrons is labeled by  $\vec{r}_{12} = \vec{x}_1 - \vec{x}_2 = \vec{s}_1 - \vec{s}_2$ . Further, in the entrance channel, let  $\vec{r}_i$  be the relative vector of  $Z_P$  with respect to the center of mass of  $(Z_T; e_1, e_2)_i$ . Likewise, in the exit channel let  $\vec{r}_f$  be the position vector between the center of mass of the  $(Z_P, e_1)_{f_1}$  and  $(Z_T, e_2)_{f_2}$  systems. The relative vectors for the configuration in the entrance channel are also visualized schematically in Fig. 1.

The unperturbed initial channel state  $\Phi_i$  is defined by  $\Phi_i = \varphi_i(\vec{x}_1, \vec{x}_2) e^{i\vec{k}_i \cdot \vec{r}_i}$ , where  $\varphi_i(\vec{x}_1, \vec{x}_2)$  represents the two-electron bound-state wave function of the atomic target system  $(Z_T; e_1, e_2)_i$ , whereas  $\vec{k}_i$  is the initial wave vector. The exact nonrelativistic total Hamiltonian  $H$  of the collision system in (1) is defined by

$$H = -\frac{1}{2\mu_i} \nabla_{r_i}^2 - \frac{1}{2b} \nabla_{x_1}^2 - \frac{1}{2b} \nabla_{x_2}^2 + \frac{Z_P Z_T}{R} - \frac{Z_P}{s_1} - \frac{Z_P}{s_2} - \frac{Z_T}{x_1} - \frac{Z_T}{x_2} + \frac{1}{r_{12}}. \quad (2)$$

Here,  $\mu_i = M_P(M_T + 2)/(M_P + M_T + 2)$  and  $b = M_T/(M_T + 1)$ , where  $M_P$  and  $M_T$  are the masses of the projectile and target, respectively. The perturbation potential  $V_i$  and  $V_f$

in the entrance and exit channel read as

$$V_i = \frac{Z_P Z_T}{R} - \frac{Z_P}{s_1} - \frac{Z_P}{s_2}, \quad V_f = \frac{Z_P Z_T}{R} + \frac{1}{r_{12}} - \frac{Z_T}{x_1} - \frac{Z_P}{s_2}. \quad (3)$$

The first three terms in Eq. (2) represent the usual kinetic-energy operators, whereas the remaining terms are the potential-energy operators of the entire system of two electrons and two nuclei. These latter three terms are the Coulomb interactions  $Z_P Z_T/R$  (between the two nuclear charges  $Z_P$  and  $Z_T$ ),  $-Z_P/s_{1,2}$  (between  $Z_P$  and  $e_{1,2}$ ),  $-Z_T/x_{1,2}$  (between  $Z_T$  and  $e_{1,2}$ ), and  $1/r_{12}$  (between  $e_1$  and  $e_2$ ).

## B. Entrance channel

Bearing in mind the long-range nature of the Coulomb interaction, the initial unperturbed state  $\Phi_i$  in the entrance channel should be distorted even at infinite distances between the colliding aggregates. This is due to the presence of the asymptotic Coulomb repulsive interaction  $V_i^\infty = Z_P(Z_T - 2)/R \approx Z_P(Z_T - 2)/r_i$  between the projectile and the screened target nuclear charge  $Z_T - 2$ . Here,  $Z_T$  is screened by the unit charges of the two electrons  $e_1$  and  $e_2$  to become  $Z_T - 2$ . In the limit  $r_i \rightarrow \infty$ , the potential  $V_i^\infty$  is deduced from  $V_i$  which appears in (3). Here,  $Z_P(Z_T - 2)/r_i$  and  $Z_P(Z_T - 2)/R$  would be equivalent if  $r_i$  could be approximated by  $R$ . Replacement of  $R$  by  $r_i$  entails resorting to the heavy-mass approximation ( $M_T \gg 1$ ). This can be seen by using the Taylor expansion of  $1/r_i$  around  $1/R$  and retaining the first two terms. The outcome shows that  $1/R - 1/r_i$  is by a factor of  $\delta$  smaller than the short-range potential  $[R \cdot (\vec{x}_1 + \vec{x}_2)]/R^3$ , where  $\delta = 1/(M_T + 2)$ . Thus, in the mass limit  $M_T \gg 1$ , the short-range potential  $1/R - 1/r_i$  is negligibly small. Consequently, for  $M_T \gg 1$ , we have  $1/r_i \approx 1/R$ . Moreover, in the asymptotic region  $R \rightarrow \infty$ , it also follows that  $1/s_1 \approx 1/R$  and  $1/s_2 \approx 1/R$ . This implies that at  $R \rightarrow \infty$  the perturbation potential  $V_i = Z_P Z_T/R - Z_P/s_1 - Z_P/s_2$  from (3) has the following Coulombic tail  $V_i \approx Z_P Z_T/r_i - Z_P/r_i - Z_P/r_i = Z_P(Z_T - 2)/r_i$ , so that  $V_i \approx Z_P(Z_T - 2)/r_i \equiv V_i^\infty$ .

Thus, the perturbation  $V_i$  is reduced to the Coulomb potential  $V_i^\infty$  in the asymptotic region of the entrance channel. This means that the corresponding unperturbed state  $\Phi_i$  does not conform to  $V_i$ . To avoid such an inconsistency,  $\Phi_i$  must be multiplied by the distorted wave stemming from  $V_i^\infty = Z_P(Z_T - 2)/r_i$ . This is accomplished through replacement of  $\Phi_i$  by the distorted wave function  $\Phi_i^+$ :

$$\Phi_i^+ = \Phi_i \mathcal{N}^+(v_i) {}_1F_1(-i v_i, 1, i k_i r_i - i \vec{k}_i \cdot \vec{r}_i), \quad (4)$$

where the long-range distortion effects are present through the Coulomb wave function  $\mathcal{N}^+(v_i) e^{i\vec{k}_i \cdot \vec{r}_i} {}_1F_1(-i v_i, 1, i k_i r_i - i \vec{k}_i \cdot \vec{r}_i)$  for the relative motion of heavy nuclei. Here,  $\mathcal{N}^+(v_i)$  is the Coulomb normalization constant (the Coulomb density of state) given by  $\mathcal{N}^+(v_i) = e^{-\pi v_i/2} \Gamma(1 + i v_i)$ , where  $v_i = Z_P(Z_T - 2)/v$  and  $v$  is the velocity of the projectile. The symbol  $\Gamma$  stands for the standard Gamma function. In (4), we used the potential  $V_i^\infty = Z_P(Z_T - 2)/r_i$  rather than its formally equivalent eikonal form  $V_i^\infty \approx Z_P(Z_T - 2)/R$ , for the reason of working with the three independent variables  $\{\vec{r}_i, \vec{x}_1, \vec{x}_2\}$  in which the eigenvalue problem becomes completely separable. This would not be the case with the set

$\{\vec{R}, \vec{x}_1, \vec{x}_2\}$  which is not comprised of independent variables because  $\vec{R} = \vec{x}_1 - \vec{s}_1 = \vec{x}_2 - \vec{s}_2$ .

The mentioned mass approximation is usually referred to as the eikonal approximation where all the terms of the order of or smaller of the reciprocal of the heavy particle mass ( $1/M_P$  and/or  $1/M_T$ ) are neglected throughout. In particular, as we saw, this implies  $r_i \approx R$ . Physically, the eikonal approximation is associated with scattering at small angles. This is completely justified for heavy particles that, due to their large mass, predominantly scatter in a narrow forward cone. The net consequence of this effect is that the Coulomb logarithmic phase factors in the scattering states fully suffice to account for any distortion effect due to the relative motion of heavy particles. In principle, the corresponding full Coulomb waves could be kept, as done, e.g., in (4), but the difference between their contributions and those from the associated logarithmic phases would be of the order of the reciprocal of the heavy particle masses.

Unlike  $\Phi_i$ , the wave function  $\Phi_i^+$  has the proper eikonal asymptote which is denoted by  $\Phi_{i,\text{eik}}^+$ :

$$\Phi_i^+ \approx \Phi_{i,\text{eik}}^+, \quad \Phi_{i,\text{eik}}^+ = \Phi_i e^{i\nu_i \ln(k_i r_i - \vec{k}_i \cdot \vec{r}_i)}, \quad r_i \rightarrow \infty. \quad (5)$$

The replacement of  $\Phi_i$  by  $\Phi_i^+$  is dictated by the requirement of satisfying the correct asymptotic behavior of the entrance channel state. However, this is a necessary, but not a sufficient condition. The sufficient condition would be fulfilled if the total Hamiltonian could be modified so as to adjust to the replacement of  $\Phi_i$  by  $\Phi_i^+$ . As emphasized, the logarithmic Coulomb phase factor in  $\Phi_i^+$  is due to the asymptote  $V_i^\infty$  of  $V_i$ . Therefore,  $V_i^\infty$  must be subtracted from  $V_i$  in  $H$ , and this is the sought sufficient condition. Such a procedure corresponds to the following decomposition or rearrangement of the total Hamiltonian  $H$ :

$$H = H_i^d + V_i^d, \quad (6)$$

with

$$H_i^d = -\frac{1}{2\mu_i} \nabla_{r_i}^2 + \frac{Z_P(Z_T - 2)}{r_i} - \frac{1}{2b} \nabla_{x_1}^2 - \frac{1}{2b} \nabla_{x_2}^2 - \frac{Z_T}{x_1} - \frac{Z_T}{x_2} + \frac{1}{r_{12}}, \quad (7)$$

where  $V_i^d$  is a model potential,

$$V_i^d \equiv V_i - V_i^\infty = \left( \frac{Z_P Z_T}{R} - \frac{Z_P}{s_1} - \frac{Z_P}{s_2} \right) - \frac{Z_P(Z_T - 2)}{r_i}. \quad (8)$$

The superscript  $d$  stands for ‘‘distortion’’ and it is introduced to indicate that the asymptotic Coulomb distortion effects are brought into the formalism. The quantity  $H_i^d$  is the noneikonalized model Hamiltonian of the entrance channel in which  $Z_T$  is free, whereas  $Z_T$ ,  $e_1$ , and  $e_2$  are bound in the initial state  $(Z_T; e_1, e_2)_i$ . The wave function  $\Phi_i^+$  from (4) is now seen to be the solution of the exact Schrödinger eigenvalue problem in the entrance channel:

$$(H_i^d - E_i) \Phi_i^+ = 0, \quad E_i = \epsilon_i + \frac{1}{2\mu_i} k_i^2, \quad (9)$$

where  $\epsilon_i$  is the binding energy of the two-electron target. The total Hamiltonian  $H$  from (6) is still exact, since we merely added and subtracted the Coulomb asymptotic tail  $V_i^\infty$  to the right-hand side of Eq. (2).

Overall, we see that the necessary and sufficient condition to fulfill the correct boundary conditions of collision in the entrance channel is secured only when *simultaneously* replacing  $\Phi_i$  by  $\Phi_i^+$  and  $V_i$  by  $V_i^d$ . This procedure from Refs. [1,5] is much simpler and, by far, more manageable in subsequent computations of the transition matrix elements than the corresponding prescription of Dollard [34], who also subtracts an operator from  $H$ . However, his Coulomb-modified Hamiltonian contains the practically unmanageable exponential function of the square root of the kinetic-energy operator.

### C. Perturbation potentials

Regarding the correct boundary conditions, it is important to determine the behavior of perturbation  $V_i^d$  at asymptotic distances  $R$  between the colliding aggregates. To this end, it suffices to consider the difference  $1/R - 1/r_i$  from  $V_i^d$  in (8). This has already been done when passing from  $V_i$  to  $V_i^\infty$ , where in the mass approximation  $M_T \gg 1$ , we have  $1/R \approx 1/r_i$ . In the same vein, we have  $V_i^d = Z_P Z_T / R - Z_P(Z_T - 2)/r_i - Z_P/s_1 - Z_P/s_2 \approx 2Z_P/R - Z_P/s_1 - Z_P/s_2$ , so that  $V_i^d \approx Z_P[(1/R - 1/s_1) + (1/R - 1/s_2)]$ . Since both  $1/R - 1/s_1$  and  $1/R - 1/s_2$  are of a short range at  $R \rightarrow \infty$ , it follows that  $V_i^d$  also behaves as a short-range potential at infinitely large distances between the two aggregates. All told, within the heavy-mass limit, the perturbation  $V_i^d$  in the entrance channel can be replaced by its eikonal counterpart which is labeled by  $V_{i,\text{eik}}^d$ :

$$V_i^d \approx V_{i,\text{eik}}^d, \quad V_{i,\text{eik}}^d = V_{\text{PR}} + V_{\text{P1}} + V_{\text{P2}} \\ V_{\text{PR}} = \frac{2Z_P}{R}, \quad V_{\text{P1}} = -\frac{Z_P}{s_1}, \quad V_{\text{P2}} = -\frac{Z_P}{s_2}. \quad (10)$$

The complete perturbation  $V_{i,\text{eik}}^d$  from (10) contains three Coulomb electrostatic interactions. Therein, the repulsive potential  $V_{\text{PR}} = 2Z_P/R$  describes the Rutherford scattering which dominates at larger scattering angles in differential cross sections. Potential  $V_{\text{P1}} = -Z_P/s_1$  is the Coulomb interaction between  $Z_P$  and the active target electron  $e_1$ . Interaction  $V_{\text{P2}} = -Z_P/s_2$  is the Coulomb potential between  $Z_P$  and the passive target electron  $e_2$ . Combined together, the perturbation  $V_{\text{P1}}$  and the confluent hypergeometric functions  ${}_1F_1(i\nu_T, 1, i\nu_T x_1 + i\vec{\nu} \cdot \vec{x}_1)$  with  $\nu_T = (Z_T - 1)/v$  from the corresponding Coulomb wave centered at  $Z_T - 1$  give the contribution from double scattering effects. Such effects are a quantum-mechanical counterpart of the classical Thomas billiard-type  $Z_P - e_1 - Z_T$  collisions. The result is the Thomas peak at  $\theta_{\text{lab}} = (1/M_P) \sin(60^\circ) \simeq 0.47$  mrad in the angular distribution within the laboratory reference system.

Potential  $V_{\text{P2}}$  in (10) also describes capture of electron  $e_1$ . However, here the nuclear charge  $Z_P$  first interacts with  $e_2$  via  $V_{\text{P2}}$  and, in the end, it is the electron  $e_1$  which is captured by the projectile. This is mediated by the static correlations of the two electrons in the bound state of the heliumlike wave function  $\varphi_i(\vec{x}_1, \vec{x}_2)$ . Such an effect coupled with the influence of

the Coulomb wave functions yields the second Thomas peak at the same angle  $\theta_{\text{lab}} \approx 0.47$  mrad. Thus, for single charge exchange (1), at sufficiently high impact energies, differential cross sections computed using (25) should clearly exhibit two double-scattering effects with two pronounced peaks for two Thomas processes ( $Z_P - e_1 - Z_T$  and  $Z_P - e_1^S - e_2^S$ ). The superscript  $S$  on the two electrons in the Thomas process  $Z_P - e_1^S - e_2^S$  is used to indicate that this Thomas peak is enabled by the static correlations of electrons in the target wave function  $\varphi_i(\vec{x}_1, \vec{x}_2)$ . This nomenclature is adopted to avoid a potential confusion of the described Thomas process  $Z_P - e_1^S - e_2^S$  with the Thomas process  $Z_P - e_1 - e_2$  in which  $Z_P$  scatters first on  $e_1$ , which subsequently collides with  $e_2$  and thus becomes captured by the projectile. Such a Thomas process is mediated by the dynamic correlations in which the Coulomb repulsion  $V_{12} = 1/r_{12}$  is directly included.

#### D. Exit channel

The analysis in the exit channel is similar to the initial channel as far as the correct boundary conditions are concerned. Here, however, the BCIS-4B method accounts for an additional effect and this is intermediate ionization of electron  $e_1$ . This can be accomplished in, e.g., exactly the same manner as in the four-body continuum distorted wave (CDW-4B) method [37]. Thus, the BCIS-4B method uses the same exit channel wave function as in the CDW-4B method:

$$\Phi_f^- = \Phi_f \mathcal{N}^-(\nu) N^-(\nu_T) {}_1F_1(-i\nu_T, 1, -i\nu x_1 - i\vec{\nu} \cdot \vec{x}_1) \times {}_1F_1(i\nu, 1, -ik_f r_f + i\vec{k}_f \cdot \vec{r}_f), \quad (11)$$

where  $\Phi_f$  is the unperturbed final state  $\Phi_f = \varphi_P(\vec{s}_1) \varphi_T(\vec{x}_2) e^{-i\vec{k}_f \cdot \vec{r}_f}$ . Here,  $N^-(\nu_T) = e^{\pi\nu_T/2} \Gamma(1 + i\nu_T)$ ,  $\mathcal{N}^-(\nu) = e^{-\pi\nu/2} \Gamma(1 - i\nu)$ , and  $\nu = Z_P(Z_T - 1)/v$ . The function  $N^-(\nu_T) {}_1F_1(-i\nu_T, 1, -i\nu x_1 - i\vec{\nu} \cdot \vec{x}_1)$  in  $\Phi_f^-$  is a part of the electronic continuum Coulomb wave function in the attractive electrostatic field  $V_{T1}^- = -(Z_T - 1)/x_1$ . The quantity  $Z_T - 1$  represents the charge of the screened target nucleus, i.e., of the target core  $(Z_T, e_2)_{f_2}$ . This screening is introduced because at infinitely large values of  $x_1$ , the captured electron  $e_1$  from  $(Z_P, e_1)_{f_1}$  cannot discern the individual constituents in the target rest  $(Z_T, e_2)_{f_2}$ . In other words, at  $x_1 \rightarrow \infty$ , the electron sees the hydrogenlike system  $(Z_T, e_2)_{f_2}$  as a point charge  $Z_T - 1$ . The state  $\Phi_f^-$  possesses the correct asymptote in its eikonal form  $\Phi_{f,\text{eik}}^-$  given by

$$\Phi_f^- \approx \Phi_{f,\text{eik}}^-, \quad \Phi_{f,\text{eik}}^- = \Phi_f e^{-i\nu \ln(k_f r_f - \vec{k}_f \cdot \vec{r}_f)} N^-(\nu_T) \times {}_1F_1(-i\nu_T, 1, -i\nu x_1 - i\vec{\nu} \cdot \vec{x}_1), \quad r_f \rightarrow \infty. \quad (12)$$

#### E. Heliumlike bound-state wave functions

The post version of the BCIS-4B method has the perturbation potential  $V_f$ , which explicitly contains the  $e_1 - e_2$  interaction  $1/r_{12}$  as per (3). This version of the theory possesses both the static and dynamic correlations. Static correlations are those present in the heliumlike wave function  $\varphi_i(\vec{x}_1, \vec{x}_2)$  with no necessary reference to any collision. Thus, the static correlations of electrons are of a spectroscopic nature. The dynamic correlations are those present in the

perturbation potentials that cause the transition in a collision. The static correlations are also included in the prior variant of the BCIS-4B method, but not the dynamic correlations, since the electronic repulsion  $1/r_{12}$  is not a part of the complete perturbation  $V_{i,\text{eik}}^d$  in (10). Of course, both the static and dynamic correlations are due to the same Coulomb repulsion ( $1/r_{12}$ ) of the two electrons  $e_1$  and  $e_2$ .

Static correlations can be included, e.g., using the wave function which explicitly contains the coordinate  $r_{12}$  :

$$\varphi_i(\vec{x}_1, \vec{x}_2) = \sum_{k_1, k_2, k_3}^{k_1+k_2+k_3 \leq K} A_{k_1, k_2, k_3} x_{12}^{k_3} \times (x_1^{k_1} x_2^{k_2} e^{-a_1 x_1 - a_2 x_2} + x_2^{k_1} x_1^{k_2} e^{-a_1 x_2 - a_2 x_1}), \quad (13)$$

where  $K$  is the total number of terms. Another alternative is to employ the concept of configuration interactions (CIs). These involve a linear combination of the products of one-electron radial orbitals dependent only on  $x_1$  and  $x_2$  multiplied altogether by the Legendre polynomial  $P_l(\cos \theta_{12}) \equiv P_l(\cos(\vec{x}_1 \cdot \vec{x}_2))$  as a function of the angle  $\theta_{12}$  between  $\vec{x}_1$  and  $\vec{x}_2$  [38]:

$$\varphi_i(\vec{x}_1, \vec{x}_2) = \frac{1}{4\pi} \sum_{\lambda=0}^L R(x_1, x_2) P_\lambda(\cos \theta_{12}), \quad (14)$$

$$R(x_1, x_2) = \sum_{k_1, k_2; k_1 \leq k_2}^{k_1+k_2 \leq k_{\text{max}}} B_{\lambda, k_1, k_2} x_1^{\lambda} x_2^{\lambda} \times (x_1^{k_1} x_2^{k_2} e^{-b_1 x_1 - b_2 x_2} + x_2^{k_1} x_1^{k_2} e^{-b_1 x_2 - b_2 x_1}). \quad (15)$$

Here,  $L$  is the maximal value of the angular momentum quantum number, whereas  $B_{\lambda, k_1, k_2}$  are linear and  $\{b_1, b_2\}$  are nonlinear variational parameters. For  $L = 3$ ,  $b_1 = b_2$ ,  $k_{\text{max}} = 6$  and with 109 parameters in the CI wave function (14), the binding energy is found to be  $\epsilon_i = -2.90267$  [38]. This estimate, which remarkably accounts for 97% of the correlation energy, is in excellent agreement with the corresponding value  $\epsilon_i = -2.9037243770$  obtained by Drake [39] using (13) with  $K = 8$  and 269 parameters. Moreover, in Ref. [39], the accuracy of  $\epsilon_i$  has been increased to a fascinating 21 decimals for  $K = 20$  and 2358 parameters. We see, however, that even without an explicit inclusion of  $\vec{r}_{12}$ , the CI wave function (14) can still accurately account for both radial and angular correlations of the two electrons in heliumlike atoms. It should be noted that the significant improvements in the accuracy of the estimates of the binding energies of heliumlike systems do not necessarily imply that similarly marked effects are to be expected in single charge exchange cross sections computed by way of the associated highly correlated wave functions. Actually, the abundant practice [2,6,36] has shown that the much simpler helium wave functions containing barely few parameters and exhibiting only radial correlations suffice to describe single-electron capture processes. For small-angle scattering, charge exchange cross sections are principally determined by the initial and final distributions of velocities of electrons around both Coulomb centers. The final velocity distributions of electrons bound to two hydrogenlike systems in process (1) are quantum-mechanically exact. As to the momentum space representations of relatively simple few parameter wave functions of heliumlike atomic systems they are also

able to provide reasonable good electronic distributions of velocities in the initial state of the target, and thus secure an adequate contribution to charge exchange cross sections for process (1). The practical utility of the CI wave functions for multielectron atomic systems is that they facilitate analytical or semianalytical calculations of bound-free form factors, much in the same fashion as in the case of single charge exchange in purely three-body collisions involving only the hydrogenlike wave functions of one-electron atomic systems. This has been illustrated by Belkić [3,40,41] for single ionization in the  $H^+ - H^-(1s^2)$  collision using the highly correlated CI wave function of  $H^-$  with some 61 variational parameters [38] in the four-body modified Coulomb-Born (MCB-4B), or equivalently, the four-body continuum distorted wave and eikonal initial state (CDW-EIS-4B) method.

The use of either (13) or the fully correlated (both radially and angularly) CI wave function (14) is very computer-time consuming for four-body single charge exchange treated by the BCIS-4B method. Instead, we shall employ a simpler alternative with only radially correlated CI wave functions for heliumlike system. In these functions, the angular momentum is equal to zero and the only present radial correlations are manifested in the exponential damping and the coefficients of the linear combination of one-electron radial orbitals. Specifically, for the initial ground state of a two-electron target, we choose the following factorized form CI wave function:

$$\varphi_i(\vec{x}_1, \vec{x}_2) = \sum_{k,l} \varphi_{\alpha_k}(\vec{x}_1) \varphi_{\alpha_l}(\vec{x}_2), \quad (16)$$

where  $\varphi_{\alpha_j}(\vec{r}) = N_{\alpha_j} \exp(-\alpha_j r)$ ,  $N_{\alpha_j} = a_j \sqrt{N}$  ( $j = k, l$ ), and  $N$  is the normalization constant. The values of the summation indices  $k$  and  $l$ , as well as the variationally determined parameters  $\alpha_j$  and  $a_j$  depend on the concrete choice of the wave function.

Such a generic form encompasses a number of the existing wave functions proposed by different authors, e.g., as follows:

(i) The one-parameter wave function of Hylleraas [42]:

$$\varphi_i(\vec{x}_1, \vec{x}_2) = \frac{\alpha^3}{\pi} e^{-\alpha(x_1+x_2)}, \quad (17)$$

where  $\alpha = 1.6875$  for helium with the binding energy  $\epsilon_i = -2.847656$ .

(ii) The two-parameter wave function of Eckart [43] or Silverman *et al.* [44]:

$$\varphi_i(\vec{x}_1, \vec{x}_2) = N(e^{-\alpha_1 x_1 - \alpha_2 x_2} + e^{-\alpha_2 x_1 - \alpha_1 x_2}), \quad (18)$$

with  $\alpha_1 = 2.183171$  and  $\alpha_2 = 1.18853$  for helium and  $\epsilon_i = -2.8756614$ .

(iii) The three-parameter function of Green *et al.* [45]:  $\varphi_i(\vec{x}_1, \vec{x}_2) = N(e^{-\alpha_1 x_1} + a e^{-\alpha_2 x_1})(e^{-\alpha_1 x_2} + a e^{-\alpha_2 x_2})$  where  $a = 0.6$ ,  $\alpha_1 = 1.455799$  and  $\alpha_2 = 2.911598$  for helium with the binding energy  $\epsilon_i = -2.86167$ .

(iv) The four-parameter wave function of Löwdin [46]:  $\varphi_i(\vec{x}_1, \vec{x}_2) = N(a_1 e^{-\alpha_1 x_1} + a_2 e^{-\alpha_2 x_1})(a_1 e^{-\alpha_1 x_2} + a_2 e^{-\alpha_2 x_2})$ , where  $a_1 = 2.7626$ ,  $a_2 = 1.9104$ ,  $\alpha_1 = 1.4287$ ,  $\alpha_2 = 2.7022$  for helium and  $\epsilon_i = -2.861525$ .

(v) The four-parameter wave function of Byron and Joachain [47] (an analytical fit to the numerically given Hartree-Fock wave function):  $\varphi_i(\vec{x}_1, \vec{x}_2) = \varphi(x_1)\varphi(x_2)$  where

$\varphi(x) = (1/\sqrt{4\pi})(Ae^{-\alpha x} + Be^{-\beta x})$  with  $A = 2.60505$ ,  $B = 2.08144$ ,  $\alpha = 1.41$  and  $\beta = 2.61$  for helium and  $\epsilon_i = -2.86167$ .

## F. Transition amplitude

As discussed, a consistent application of the eikonal approximation requires neglecting every term of the order of or less than the reciprocal of the mass of heavy nuclei. This amounts to the use of the corresponding eikonal forms of the channel wave functions and perturbation potentials according to

$$\Phi_i^+ \approx \Phi_{i,\text{eik}}^+, \quad V_i^d \approx V_{i,\text{eik}}^d, \quad \Phi_f^- \approx \Phi_{f,\text{eik}}^-. \quad (19)$$

With such a coherent setting, the prior form of the eikonal transition amplitude in the BCIS-4B method is given by

$$T_{\text{if}} = \langle \Phi_{f,\text{eik}}^- | V_{i,\text{eik}}^d | \Phi_{i,\text{eik}}^+ \rangle. \quad (20)$$

Advantageously, by employing the eikonal approximation, the product of the logarithmic Coulomb factors from the wave functions  $\Phi_{i,\text{eik}}^+$  and  $\Phi_{f,\text{eik}}^-$  can be reduced to a single phase:

$$\begin{aligned} & \exp[i v_i \ln(k_i r_i - \vec{k}_i \cdot \vec{r}_i) + i v \ln(k_f r_f - \vec{k}_f \cdot \vec{r}_f)] \\ & \approx \exp[i v_i \ln(v R - \vec{v} \cdot \vec{R}) + i v \ln(v R + \vec{v} \cdot \vec{R})] \\ & = (\rho v)^{2i v_i} (v R + \vec{v} \cdot \vec{R})^{i \xi}, \end{aligned} \quad (21)$$

where  $\xi = Z_p/v$  and  $\vec{\rho}$  is the projection of vector  $\vec{R}$  onto the  $XOY$  plane ( $\vec{\rho} = \vec{R} - \vec{Z}$ ,  $\vec{\rho} \cdot \vec{Z} = 0$ ). The overall phase factor  $(\rho v)^{2i v_i} \equiv (\rho v)^{2i Z_p(Z_T-2)/v}$  is due to the Coulomb repulsion between  $Z_p$  and  $Z_T - 2$ . This latter multiplying term  $(\rho v)^{2i v_i}$  does not contribute to the total cross section for any values of  $Z_p$  and  $Z_T$ . Such a feature is not limited to the BCIS-4B method. Namely, Belkić *et al.* [1] have shown that it holds true in the case of the exact eikonal transition amplitude for charge exchange. Evidently, in the special case with helium as a target ( $Z_T = 2$ ), the same phase  $(\rho v)^{2i Z_p(Z_T-2)/v}$  reduces to unity and, as such, makes no contribution whatsoever. This latter situation with a helium target is especially convenient for computations of differential cross sections in the CB1-4B and BCIS-4B methods because for  $(\rho v)^{2i Z_p(Z_T-2)/v} = 1$  the defining angular distributions become directly proportional to the absolute value squared of the transition amplitudes with no need to carry out any additional quadrature.

Overall, within the consistent eikonal approximation valid at the small-angle collisions of heavy particles, we have

$$\vec{k}_i \cdot \vec{r}_i + \vec{k}_f \cdot \vec{r}_f = \vec{\alpha} \cdot \vec{s}_1 + \vec{\beta} \cdot \vec{x}_1 = -\vec{v} \cdot \vec{x}_1 - \vec{\alpha} \cdot \vec{R}, \quad (22)$$

where the two momentum transfers  $\vec{\alpha}$  and  $\vec{\beta}$  are

$$\vec{\beta} = -\vec{\eta} - \beta_z \hat{v}, \quad \vec{\alpha} = \vec{\eta} - \alpha_z \hat{v}, \quad \vec{\alpha} + \vec{\beta} = -\vec{v}, \quad (23)$$

$$\alpha_z = \frac{v}{2} - \frac{\Delta E}{v}, \quad \beta_z = \frac{v}{2} + \frac{\Delta E}{v}, \quad (24)$$

with  $\Delta E = \epsilon_i - \epsilon_f$  and  $\epsilon_f = -Z_p^2/2 - Z_T^2/2$ . The transverse component of the change in the relative linear momentum of a heavy particle is denoted by  $\vec{\eta} = (\eta \cos \phi_\eta, \eta \sin \phi_\eta, 0)$  where  $\vec{\eta} \cdot \vec{v} = 0$ .

Therefore, the prior form of the eikonal transition amplitude in the BCIS-4B approximation for process (1) becomes

$$T_{if}(\vec{\eta}) = [N^-(\nu_T)]^* \iiint d\vec{x}_1 d\vec{x}_2 d\vec{R} \varphi_P^*(\vec{s}_1) \varphi_T^*(\vec{x}_2) \times \left( \frac{2Z_P}{R} - \frac{Z_P}{s_1} - \frac{Z_P}{s_2} \right) \varphi_i(\vec{x}_1, \vec{x}_2) e^{-i\vec{a} \cdot \vec{R} - i\vec{v} \cdot \vec{x}_1} \times {}_1F_1(i\nu_T, 1, i\nu x_1 + i\vec{v} \cdot \vec{x}_1) (vR + \vec{v} \cdot \vec{R})^{i\xi}. \quad (25)$$

Notice that the CB1-4B method can formally be obtained from Eq. (25), first through the replacement of the confluent hypergeometric function  $N^-(\nu_T) {}_1F_1(-i\nu_T, 1, -i\nu x_1 - i\vec{v} \cdot \vec{x}_1)$  by its asymptotic form  $\exp[i\nu_T \ln(\nu x_1 + \vec{v} \cdot \vec{x}_1)]$  and then via the use of the limit  $t \rightarrow \infty$  as  $\lim_{t \rightarrow \infty} (\nu x_1 + \vec{v} \cdot \vec{x}_1) = \lim_{t \rightarrow \infty} (vR + v^2 t)$ . This latter step is due to the fact that  $\vec{x}_1$  is indistinguishable from  $\vec{R}$  at  $t \rightarrow \infty$ .

The prior form of the transition amplitude  $T_{if}(\vec{\eta})$  from Eq. (25) can be interpreted in the following plausible way. In the entrance channel, the collision between the projectile  $P$  and target ( $T, 2e$ ) results in an accumulation of the Coulombic phase factor  $\exp[(i/v)Z_P(Z_T - 2) \ln(vR - \vec{v} \cdot \vec{R})]$ . On the other hand, in the exit channel, the scattered projectile  $P$  interacts with the screened target nucleus accumulating the phase factor  $\exp[-(i/v)Z_P(Z_T - 1) \ln(vR + \vec{v} \cdot \vec{R})]$ . At the same time, the interaction of  $P$  with the target leads to single ionization of the target ( $T, 2e$ ). The ionized electron propagates in the Coulomb field of charge  $Z_T - 1$  in a particular direction with the momentum  $\vec{k} = \vec{v}$ . Finally, capture of the electron occurs from these intermediate ionizing states (capture from the continuum) because the electron is traveling together with the projectile in the same direction and the attractive Coulomb interaction between  $Z_P$  and  $e_1$  is sufficient to bind them together into the hydrogenlike atomic system ( $Z_P, e_1$ )<sub>f<sub>1</sub></sub>.

It is interesting to see how different second-order methods conceive certain quantum-mechanical counterparts of the classical Thomas double scattering [1]. For example, in the four-body boundary-corrected second Born (CB2-4B) method [6], the Thomas process  $Z_P - e_1 - Z_T$  has its quantum-mechanical analog in the transition operator  $V_{P1} G_0 V_{T1}$ , where  $G_0$  is the free-particle Green or resolvent operator. Here, one of double scatterings is present by way of two potentials  $V_{P1}$  and  $V_{T1}$  on each side of  $G_0$ . By comparison, in the BCIS-4B method, instead of the second-order transition operator  $V_{P1} G_0 V_{T1}$ , we have the first-order transition operator  $V_{i,eik}^d$  in (3), which is in (25) taken between the Coulomb-distorted channel wave functions  $\Phi_{i,eik}^+$  and  $\Phi_{f,eik}^-$ . Nevertheless, the two different Coulomb centers, necessary for the Thomas double scattering, are also actively involved in the BCIS-4B method. One is via the projectile nuclear charge  $Z_P$  in  $V_{i,eik}^d$ . The other is through the screened nuclear charge  $Z_T - 1$  in the electronic Coulomb wave function from  $\Phi_{f,eik}^-$ . Thus, the physics of the Thomas mechanism for double collisions  $Z_P - e_1 - Z_T$  in the prior BCIS-4B method proceeds first by having  $Z_P$  scattered off the electron  $e_1$  via the potential  $V_{P1} = -Z_P/s_1$ . As a result,  $e_1$  is deflected towards the point charge  $Z_T - 1$  the interaction with which, by way of the potential  $V'_{T1} = -(Z_T - 1)/x_1$ , leads to emission of  $e_1$  into the state described by the Coulomb wave centered on the screened nuclear charge  $Z_T - 1$  of the target rest ( $Z_T, e_2$ )<sub>f<sub>2</sub></sub> in the exit channel.

In Eq. (25), it will prove convenient to express the confluent hypergeometric function (the Kummer function)  ${}_1F_1(i\nu_T, 1, i\nu x_1 + i\vec{v} \cdot \vec{x}_1)$  as the following integral representation:

$${}_1F_1(i\nu_T, 1, i\nu x_1 + i\vec{v} \cdot \vec{x}_1) = \frac{1}{\Gamma(i\nu_T)\Gamma(1 - i\nu_T)} \int_0^1 d\tau \tau^{i\nu_T - 1} (1 - \tau)^{-i\nu_T} e^{i(\nu x_1 + \vec{v} \cdot \vec{x}_1)\tau}, \quad (26)$$

where an infinitesimally small negative imaginary part  $-i\epsilon$  ( $\epsilon > 0$ ) is assumed to be implicitly added to the parameter  $\nu_T \rightarrow \nu_T - i\epsilon$  in order to secure the convergence of the integral. Upon carrying out the calculation, the limit  $\epsilon \rightarrow 0^+$  should be taken. This procedure is necessary since the integral representation

$${}_1F_1(a, c, z) = \frac{\Gamma(c)}{\Gamma(a)\Gamma(c - a)} \int_0^1 dt t^{a-1} (1 - t)^{c-a-1} e^{zt} \quad (27)$$

is valid only for  $\text{Re}(c) > \text{Re}(a) > 0$  and  $\text{arg} t = \text{arg}(1 - t) = 0$ . Thus, the transition amplitude can be written in the following concise form:

$$T_{if} = M \int_0^1 d\tau f(\tau) S_{if}(\tau), \quad (28)$$

where

$$f(\tau) = \tau^{i\nu_T - 1} (1 - \tau)^{-i\nu_T}, \quad M = \frac{[N^-]^*}{\Gamma(i\nu_T)\Gamma(1 - i\nu_T)}, \quad (29)$$

$$S_{if}(\tau) = \sum_{k,l} N_{\alpha_k} N_{\alpha_l} \int d\vec{R} e^{i\vec{\beta} \cdot \vec{R}} (vR + \vec{v} \cdot \vec{R})^{i\xi} \mathcal{T}(\vec{R}), \quad (30)$$

$$\begin{aligned} \mathcal{T}(\vec{R}) &= \iint d\vec{s}_1 d\vec{s}_2 \varphi_P^*(\vec{s}_1) \varphi_T^*(\vec{x}_2) e^{-i\vec{v} \cdot \vec{s}_1} \\ &\times \left( \frac{2Z_P}{R} - \frac{Z_P}{s_1} - \frac{Z_P}{s_2} \right) e^{-\alpha_l x_2} \Psi_k(\vec{x}_1) \\ &= Z_P \left[ \frac{2}{R} W_R^{(k,l)} - W_{s_1}^{(k,l)} - W_{s_2}^{(k,l)} \right], \end{aligned} \quad (31)$$

$$\Psi_k(\vec{x}_1) = e^{-\alpha_k x_1} e^{i(\nu x_1 + \vec{v} \cdot \vec{x}_1)\tau}, \quad (32)$$

$$W_R^{(k,l)} = \mathcal{A}_k \mathcal{C}_l, \quad W_{s_1}^{(k,l)} = \mathcal{B}_k \mathcal{C}_l, \quad W_{s_2}^{(k,l)} = \mathcal{A}_k \mathcal{D}_l. \quad (33)$$

The explicit expressions for the quantities  $\mathcal{A}_k$ ,  $\mathcal{B}_k$ ,  $\mathcal{C}_l$ , and  $\mathcal{D}_l$  are derived in Appendix A. By employing the results from Appendix A, we arrived at the following final form for the transition amplitude  $T_{if}$  in terms of the two-dimensional integral over real variables  $\tau$  and  $t$ :

$$\begin{aligned} T_{if} &= 16\pi^2 Z_P^{5/2} Z_T^{3/2} \Gamma(1 + i\xi) M \sum_{k,l} N_{\alpha_k} N_{\alpha_l} \int_0^1 d\tau f(\tau) \frac{\mu_1}{\zeta^3} \\ &\times \int_0^1 dt \frac{1-t}{\Delta_1^3} (v_1 - i\xi \delta_1), \end{aligned} \quad (34)$$

where  $\nu_1 = \nu_2 + \nu_3$  and  $\delta_1 = \delta_2 + \delta_3$ ,

$$\nu_2 = 4\mathcal{F}^{(\Delta_1)}[3p+2(3p\Delta_1-1)D^{(\Delta_1)}-2(p\Delta_1-1)D^{(\Delta_1)}A_\alpha^{(\Delta_1)}], \quad (35)$$

$$\nu_3 = 4p\mathcal{F}^{(\Delta)} \left[ 3 + 3(\zeta + 2\Delta_1)D^{(\Delta)} - \Delta_1(3\zeta + 2\Delta_1)D^{(\Delta)} \right. \\ \left. \times \frac{A_\alpha^{(\Delta)}}{\Delta} - 2\zeta\Delta_1^2(D^{(\Delta)})^2 \frac{A_\beta^{(\Delta)}}{\Delta} \right], \quad (36)$$

$$\delta_2 = 4\mathcal{F}^{(\Delta_1)}[2(3p\Delta_1 - 1)D^{(\Delta_1)}C^{(\Delta_1)} \\ + 2(p\Delta_1 - 1)D^{(\Delta_1)}B_\alpha^{(\Delta_1)}], \quad (37)$$

$$\delta_3 = 4p\mathcal{F}^{(\Delta)} \left[ 3(\zeta + 2\Delta_1)D^{(\Delta)}C^{(\Delta)} + \Delta_1(3\zeta + 2\Delta_1)D^{(\Delta)} \right. \\ \left. \times \frac{B_\alpha^{(\Delta)}}{\Delta} + 2\zeta\Delta_1^2(D^{(\Delta)})^2 \frac{B_\beta^{(\Delta)}}{\Delta} \right]. \quad (38)$$

---


$$I = \frac{1}{\Gamma(i\nu_T)\Gamma(1-i\nu_T)} \left\{ \int_0^1 d\tau \left( \frac{\tau}{1-\tau} \right)^{i\nu_T} \frac{F(\tau) - \tau F_{1,0} - F(0)}{\tau} + F_{1,0} \int_0^1 d\tau \left( \frac{\tau}{1-\tau} \right)^{i\nu_T} + F(0) \int_0^1 d\tau \left( \frac{\tau}{1-\tau} \right)^{i\nu_T} \frac{1}{\tau} \right\}, \quad (40)$$

where  $F_{1,0} = F(1) - F(0)$ . This Cauchy procedure for simultaneous regularization of two branch-points singularities implies

$$I = F(0) + i\nu_T F_{1,0} + \frac{i \sinh(\pi\nu_T)}{\pi} \int_0^1 d\tau \left( \frac{\tau}{1-\tau} \right)^{i\nu_T} \\ \times \frac{F(\tau) - \tau F_{1,0} - F(0)}{\tau}. \quad (41)$$

Here, we have employed the following properties of the  $\gamma$  function:  $\int_0^1 dt t^{p-1}(1-t)^{q-1} = \Gamma(p)\Gamma(q)/\Gamma(p+q)$ ,  $\Gamma(i\nu)\Gamma(1-i\nu) = -i\pi/\sinh(\pi\nu)$ , and  $\Gamma(1+i\nu) = i\nu\Gamma(i\nu)$ . The regularized integration over  $\tau$  in Eq. (41) is now smooth and thus well adapted for the application of the Gauss-Legendre numerical quadrature.

#### H. Dominance of forward scattering for heavy particles

After the outlined Cauchy regularization, the computations of differential ( $dQ/d\Omega$ ) and total ( $Q$ ) cross sections become feasible. These latter two cross sections are defined by

$$\frac{dQ}{d\Omega}(a_0^2/sr) = \frac{\mu^2}{4\pi^2} |T_{if}(\vec{\eta})|^2, \quad (42)$$

$$Q(\pi a_0^2) = \frac{1}{2\pi^2 v^2} \int_0^\infty d\eta \eta |T_{if}(\vec{\eta})|^2, \quad (43)$$

where  $\mu = M_T M_P / (M_T + M_P)$  is the reduced mass of the incident and target nuclei of mass  $M_P$  and  $M_T$ . In the computations of the total cross sections from (43), three-dimensional quadratures must be performed numerically.

The formulas for the quantities appearing in  $\nu_2$ ,  $\nu_3$ ,  $\delta_2$ , and  $\delta_3$  are given in Appendix A.

#### G. Cauchy regularization of two branch point singularities

The expression for the transition amplitude  $T_{if}$  given by Eq. (34) requires a numerical computation of an integral of the type

$$I = \frac{1}{\Gamma(i\nu_T)\Gamma(1-i\nu_T)} \int_0^1 d\tau \tau^{i\nu_T-1} (1-\tau)^{-i\nu_T} F(\tau), \quad (39)$$

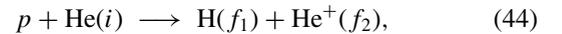
where  $F(\tau)$  is a regular, analytical function. It is well known that the Gaussian-Legendre quadrature produces accurate results, provided that the function to be integrated can be approximated by a polynomial function within the range  $[-1, 1]$ . This quadrature method needs to be regularized for functions with singularities. The integrand in Eq. (39) possesses the integrable branch-point singularities at  $\tau = 0$  and  $\tau = 1$ , both of which are regularizable. Following Refs. [31,48], the standard Cauchy regularization of the whole integrand is done in the following way. The expression for  $I$  can be rewritten as

Throughout the computations, the Gauss-Legendre quadrature is employed for the numerical integration over  $\tau$  and  $t$ . The remaining integration over  $\eta$  is also performed by means of the Gauss-Legendre routine, after performing the change of variable  $\eta = \sqrt{2(1+z)/(1-z)}$  where  $z \in [-1, +1]$ , as suggested in Ref. [49]. This latter change is very important for heavy projectiles, since it concentrates the integration points near the forward cone which contributes dominantly to the total cross sections.

### III. RESULTS, INTERPRETATIONS, AND DETAILED DISCUSSION

#### A. Illustrations for proton-helium single charge exchange

Numerical computations of the total and differential cross sections for process (1) are carried out for proton-helium charge exchange:



where  $i = \{n_i, l_i, m_i\}$  and  $f_k = \{n_{f_k}, l_{f_k}, m_{f_k}\}$  ( $k = 1, 2$ ). Further, for brevity, we shall introduce the following notation for the principal, angular, and magnetic quantum numbers of atomic hydrogen in (44):  $n \equiv n_{f_1}$ ,  $l \equiv l_{f_1}$ , and  $m \equiv m_{f_1}$ . The initial target state is taken to be the ground state of helium ( $i = 1s^2 = {}^1S$ ). Further, since no two-electron transitions are considered, the final state of the noncaptured electron in the target rest ( $\text{He}^+$ ) is taken to be the ground state ( $f_2 = \{1, 0, 0\} = 1s$ ) of the positive helium ion. As such, the general process (44) specifies to

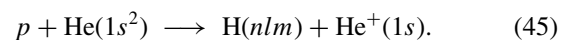


TABLE I. Total cross sections (in  $\text{cm}^2$ ) in the prior version of the BCIS-4B method (present computation) for process (45) as a function of the number of integration points used per each axis of the numerical quadrature for different incident proton energies. The initial ground state of  $\text{He}(1s^2)$  is described by means of the two-parameter wave function of Silverman *et al.* [44] from (18). The first column denoted by  $N_{\text{GL}}$  represents the number of integration points of Gauss-Legendre quadrature. Notation in square brackets denotes the power of 10 (e.g.,  $1.234567[-20]$  denotes  $1.234567 \times 10^{-20}$ ). In the eikonal approximation adopted in the present work, all the computed cross sections should normally be given with maximally three decimal places. This table is an exception with six decimals that are quoted merely to monitor the convergence pattern with the increasing value of  $N_{\text{GL}}$ .

$N_{\text{GL}}$	100 keV	500 keV	1000 keV	5000 keV	7500 keV	10000 keV
8	2.110632[-17]	5.602142[-20]	4.255470[-21]	2.782764[-23]	8.618687[-24]	3.364091[-24]
16	2.147336[-17]	6.877709[-20]	3.447023[-21]	1.911654[-24]	4.102552[-25]	3.564143[-25]
24	2.144829[-17]	7.023672[-20]	3.021237[-21]	5.862063[-25]	1.295930[-25]	1.144838[-25]
32	2.141982[-17]	7.053172[-20]	3.007754[-21]	7.199619[-25]	5.066201[-26]	1.764407[-26]
40	2.140066[-17]	7.059236[-20]	3.064864[-21]	8.355055[-25]	7.256210[-26]	1.200230[-26]
48	2.138811[-17]	7.060442[-20]	3.075047[-21]	5.618837[-25]	1.159952[-25]	1.792922[-26]
64	2.137390[-17]	7.060766[-20]	3.062222[-21]	6.419846[-25]	6.688589[-26]	1.016979[-26]
80	2.136678[-17]	7.060796[-20]	3.064503[-21]	7.214781[-25]	5.920439[-26]	1.661608[-26]
96	2.136286[-17]	7.060790[-20]	3.064159[-21]	6.224207[-25]	7.520591[-26]	1.056388[-26]
112	2.136055[-17]	7.060776[-20]	3.064216[-21]	6.146686[-25]	5.892633[-26]	1.583965[-26]
128	2.135911[-17]	7.060760[-20]	3.064214[-21]	6.606044[-25]	7.348714[-26]	1.115517[-26]
144	2.135818[-17]	7.060746[-20]	3.064217[-21]	6.461175[-25]	6.316485[-26]	1.483549[-26]
160	2.135756[-17]	7.060733[-20]	3.064218[-21]	6.293159[-25]	6.576076[-26]	1.151011[-26]
176	2.135714[-17]	7.060722[-20]	3.064218[-21]	6.401141[-25]	6.673301[-26]	1.415917[-26]
192	2.135684[-17]	7.060713[-20]	3.064219[-21]	6.452928[-25]	6.341411[-26]	1.185352[-26]
208	2.135663[-17]	7.060705[-20]	3.064219[-21]	6.380397[-25]	6.744594[-26]	1.370539[-26]
224	2.135648[-17]	7.060698[-20]	3.064219[-21]	6.377379[-25]	6.415314[-26]	1.210353[-26]
240	2.135637[-17]	7.060693[-20]	3.064218[-21]	6.414298[-25]	6.607287[-26]	1.338578[-26]
256	2.135629[-17]	7.060687[-20]	3.064218[-21]	6.403798[-25]	6.537978[-26]	1.228189[-26]
272	2.135623[-17]	7.060683[-20]	3.064218[-21]	6.388801[-25]	6.503980[-26]	1.317513[-26]
288	2.135619[-17]	7.060679[-20]	3.064218[-21]	6.398719[-25]	6.591393[-26]	1.241592[-26]
304	2.135616[-17]	7.060676[-20]	3.064218[-21]	6.403026[-25]	6.494588[-26]	1.303354[-26]
320	2.135614[-17]	7.060673[-20]	3.064218[-21]	6.396701[-25]	6.572784[-26]	1.251102[-26]
336	2.135613[-17]	7.060670[-20]	3.064218[-21]	6.396590[-25]	6.526390[-26]	1.293647[-26]
352	2.135612[-17]	7.060667[-20]	3.064218[-21]	6.399755[-25]	6.539910[-26]	1.257888[-26]
368	2.135611[-17]	7.060665[-20]	3.064217[-21]	6.398794[-25]	6.550031[-26]	1.287086[-26]

For both differential and total cross sections, the helium ground state is presently described by the two-parameter wave function (ii) of Silverman *et al.* [44] from Eq. (18). Our earlier study [36] has shown that, e.g., total cross sections for process (45), computed using the CB1-4B approximation, are practically the same for the helium wave functions (ii) and (iv) of Silverman *et al.* [44] and Löwdin [46], respectively. For all the differential and total cross sections from the BCIS-4B method, the final states of the atomic hydrogen  $\text{H}(nlm)$  are taken to be the ground state,  $\{n, l, m\} = \{1, 0, 0\} = 1s$ . The same applies to the CB1-4B method with only two exceptions, and these are the differential cross sections at the impact energies 100 keV and 7.5 MeV for which the whole manifold of the excited states ( $1 \leq n \leq 4$ ) has explicitly been taken into account, including all the possible sublevels characterized by  $l$  and  $m$ . The obtained results for differential and total cross sections from the BCIS-4B method are compared with those from the CB1-4B method as well as with the available experimental data.

### B. Total cross sections

In order to approximately include the contributions from the excited states of atomic hydrogen, the obtained total

cross sections are multiplied by 1.202. This numerical factor comes from the scaling law of Oppenheimer [50,51] for process (45) with respect to the states of atomic hydrogen  $\text{H}(n)$  where the sums over  $l$  and  $m$  are carried out (Appendix B).

Special attention has been paid to convergence during numerical integrations in order to check the effect of the above described regularization. In Table I, the results for the total cross sections are shown at six impact energies for different sets of the quadrature order  $N_{\text{GL}}$  associated with some 8–368 integration points per each integration axis ( $N_{\text{GL}}$  denotes the number of integration points of Gauss-Legendre quadrature). As expected, at lower impact energies fewer integration points are required to achieve good convergence. Particularly at the highest energies, cross sections as a function of  $N_{\text{GL}}$  are seen in Table I to oscillate. This occurs because with a large increase in the incident velocity  $v$ , the Sommerfeld parameter  $\nu_{\text{T}}$  becomes very small with the ensuing heavy oscillations of the function  $f(\tau) = \tau^{i\nu_{\text{T}}-1}(1-\tau)^{-i\nu_{\text{T}}}$  from (29) within the integral (39). Such a circumstance becomes a very challenging task for the Cauchy regularization of the integral in (41) and this, in turn, necessitates a very large number of quadrature points.

The results of the computations of total cross sections for process (45) at impact energies 20–10 000 keV are also shown

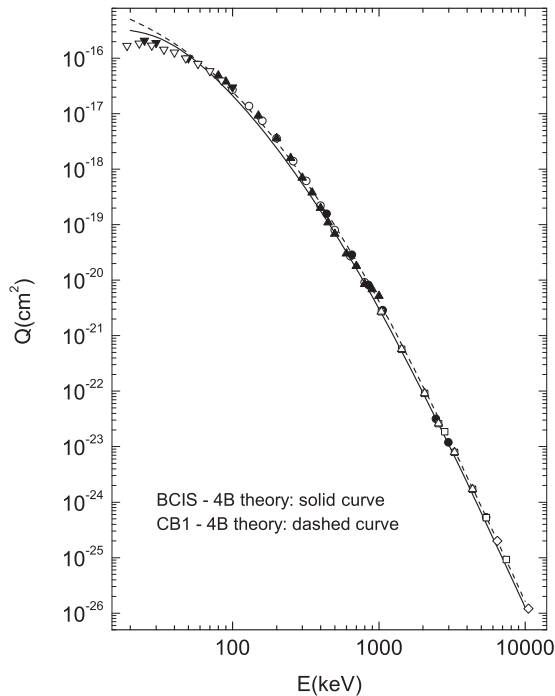


FIG. 2. Total cross sections (in  $\text{cm}^2$ ) as a function of the laboratory incident energy for process  $p + \text{He} \rightarrow \text{H} + \text{He}^+$ . The solid curve represents the prior total cross sections in the prior BCIS-4B method (present computation). The dashed curve represents the results from the prior form of the prior CB1-4B method [35]. The initial ground state of  $\text{He}(1s^2)$  is described by means of the two-parameter wave function of Silverman *et al.* [44]. The explicit computations are carried out only for the ground state of  $\text{H}(1s)$  and the Oppenheimer  $n^{-3}$  scaling law with the multiplying factor 1.202 is used for  $\text{H}(n)$  to estimate the contribution from the whole spectrum of the excited states. Experimental data:  $\nabla$  Shah *et al.* [52],  $\triangle$  Schryber [53],  $\circ$  Shah and Gilbody [54],  $\square$  Horsdal-Pedersen *et al.* [60],  $\diamond$  Berkner *et al.* [55],  $\blacktriangle$  Williams [56],  $\blacktriangledown$  Martin *et al.* [58],  $\bullet$  Welsh *et al.* [57].

by way of graphs in Fig. 2. As can be seen from Fig. 2, above 50 keV, the present results from the BCIS-4B approximation are found to be in excellent agreement with the available experimental data in an extended energy range which covers nearly three orders of magnitude (abscissa) alongside the formidable 11 orders of magnitude of cross sections (ordinate).

In order to critically assess the role of the continuum-intermediate states, a comparison with the corresponding total cross sections from the CB1-4B method is made, and this is shown in Fig. 2. Therein, both theoretical curves are obtained with the complete perturbation potential  $V_{i,\text{eik}}^d = 2Z_p/R - Z_p/s_1 - Z_p/s_2$  from (10). As mentioned, the perturbation potential  $V_{i,\text{eik}}^d$  is the same in the BCIS-4B and CB1-4B theories. However, unlike the CB1-4B approach, the BCIS-4B method takes full account of the Coulomb-intermediate states of the captured electron in the exit channel.

According to Fig. 2, the BCIS-4B method provides the total cross sections that are slightly smaller than the corresponding results of the CB1-4B method throughout the energy range under consideration. Such a pattern is explained by the following argument. Before the actual capture takes place,

the transferred electron is intermediately found in the on-shell continuum state of the Coulomb point charge  $Z_T - 1$  of the target rest  $\text{He}^+$ . Since the electron is not staying in this continuum state in the final stage of the collision, the probability for electron transfer to a discrete state in the projectile Coulomb field is reduced. The obtained reduction seen in Fig. 2 is significant.

We see that the mechanism of having one electron in the continuum-intermediate state, as in the BCIS-4B method for single charge exchange, becomes dominant over the simple picture described by the CB1-4B method. In the CB1-4B method, the captured electron is free in the intermediate stage of collision involving single charge exchange. It should be noted that the like reduction of the total cross sections due to the inclusion of continuum-intermediate states is much more pronounced in the case of double electron capture, as demonstrated by Belkić [31] for the  $\alpha + \text{He} \rightarrow \text{He} + \alpha$  collisions. The reason for this is that the prior form of the BCIS-4B method for double charge exchange contains the product of the two electronic Coulomb wave functions (one for  $e_1$  and the other for  $e_2$ ) both centered symmetrically on the target rest which is bare target nuclear charge  $Z_T$  in the exit channels.

### C. Differential cross sections

Next, we shall analyze differential cross sections. These provide a more sensitive test for theoretical methods and give more detailed information about the collision under study. The results from the BCIS-4B method together with those of the CB1-4B method for differential cross sections at intermediate impact energies 100, 150, and 300 keV, as well as at higher incident energies 1.3, 2.5, 5.0, 7.5, and 12.5 MeV are depicted in Figs. 3–10.

#### 1. Intermediate impact energies

The angular distributions, or equivalently, the differential cross sections for an incident energy of 100 keV obtained by means of the BCIS-4B method are displayed by the solid curve in Fig. 3. The theoretical results computed using the CB1-4B approximation are also shown in the same figure (dashed curve). A comparison of our results is made with the two sets of experimental measurements, one of Schöffler *et al.* [13] and the other Guo *et al.* [16]. Using the so-called reaction microscope, as the COLTRIMS technique is sometimes called, Guo *et al.* [16] have recently measured differential cross sections at 100 keV for process (45) and obtained results that are similar to those of Schöffler *et al.* [13]. This can be seen in Fig. 3. In the early 1980s, Martin *et al.* [58] reported on the differential cross sections for  $p - \text{He}$  collisions at 100 keV by using an energy-loss spectrometer. This experiment belongs to the category of measurement of so-called translational spectroscopy. The results from Ref. [58] (not shown in Fig. 3 to avoid clutter) are close to the data from Refs. [13,16]. The CB1-4B method is seen here to significantly overestimate the experimental data after the dip at larger scattering angles. This indicates that the Rutherford scattering due to the nucleus-nucleus interaction is not sufficiently countered by the potentials between the projectiles and the two electrons of the target.

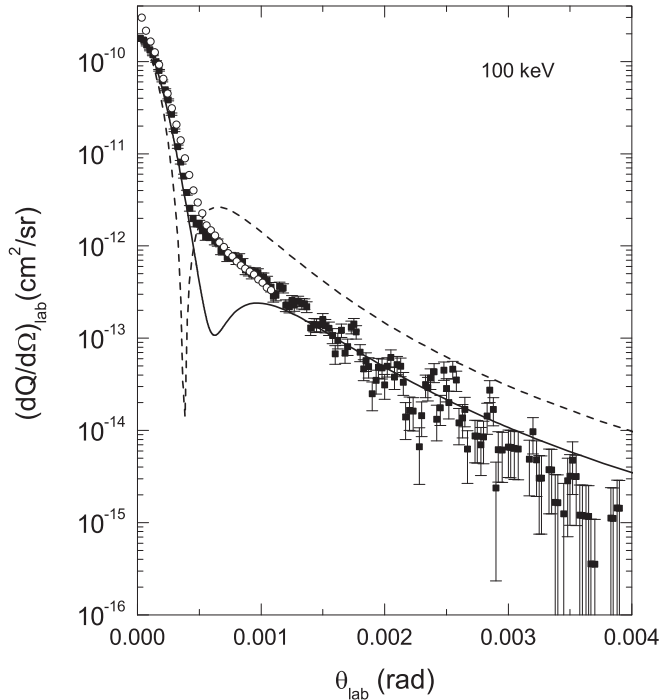


FIG. 3. Differential cross sections as a function of scattering angle  $\theta \equiv \theta_{\text{lab}}$  (rad) in the laboratory frame of reference at incident energy  $E = 100$  keV for single-electron capture by protons from  $\text{He}(1s^2)$ . The solid curve represents the theoretical results obtained by using the prior BCIS-4B method (present computations). The dashed curve represents the theoretical results of the prior CB1-4B method (present computations). The initial ground state of  $\text{He}(1s^2)$  is described by means of the two-parameter wave function of Silverman *et al.* [44]. The explicit computations are carried out only for the ground state of  $8\text{H}(1s)$  and the Oppenheimer  $n^{-3}$  scaling law with the multiplying factor 1.202 is used for  $H(n)$  to estimate the contribution from the whole spectrum of the excited states. Experimental data: ■ Schöffler *et al.* [13], ○ Guo *et al.* [16].

As can be seen from Fig. 3, both the CB1-4B and BCIS-4B methods exhibit an unphysical and experimentally unobserved dip due to a severe cancellation of the contributions from the two potentials with different signs contained in the complete perturbation  $2Z_P/R - Z_P/s_1 - Z_P/s_2$  from (10). The angle at which this dip occurs is sometimes called the dark angle. A comparison between the minima around the dark angles shows that the CB1-4B method exhibits a sharper, narrower, and deeper minimum than that from the BCIS-4B method. Except for the angular region around the dark angle, the results from the BCIS-4B method are seen to be in overall very good agreement with the experimental data of Schöffler *et al.* [13].

A similar discussion can also be made regarding Figs. 4 and 5 that deal with the incident energies of 150 and 300 keV, respectively. The disagreement between the results of the BCIS-4B and CB1-4B methods is again attributed to the influence of intermediate-continuum states that are included in the former and neglected in the latter approximation.

## 2. High impact energies and double scattering

Figures 6–10 show the angular distributions at higher energies (1.3–12.5 MeV). Therein, it is seen that the shapes

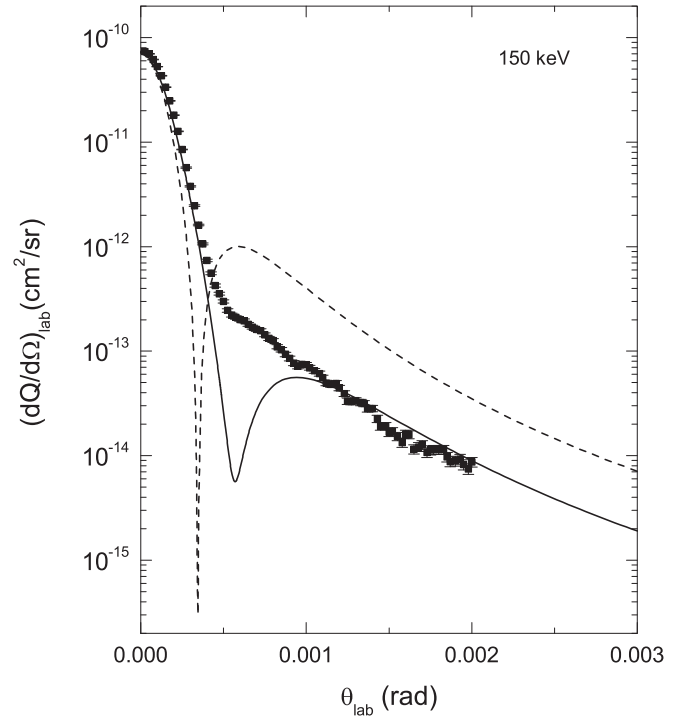


FIG. 4. The same as in Fig. 3, except for the incident energy of 150 keV.

of these differential cross sections in the BCIS-4B method are all similar to each other. They all have maxima at the forward angle ( $\theta = 0$ ) as well as at the Thomas angle located at about 0.47 mrad. The emergence of the Thomas peaks,

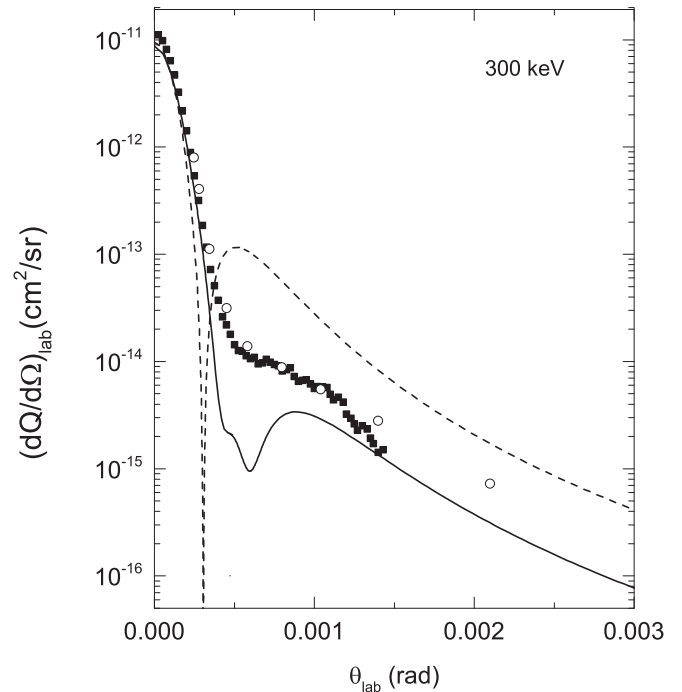


FIG. 5. The same as in Fig. 3, except for the incident energy of 300 keV and for a different measurement. Experimental data: ■ Schöffler *et al.* [13], ○ Loftager [59].

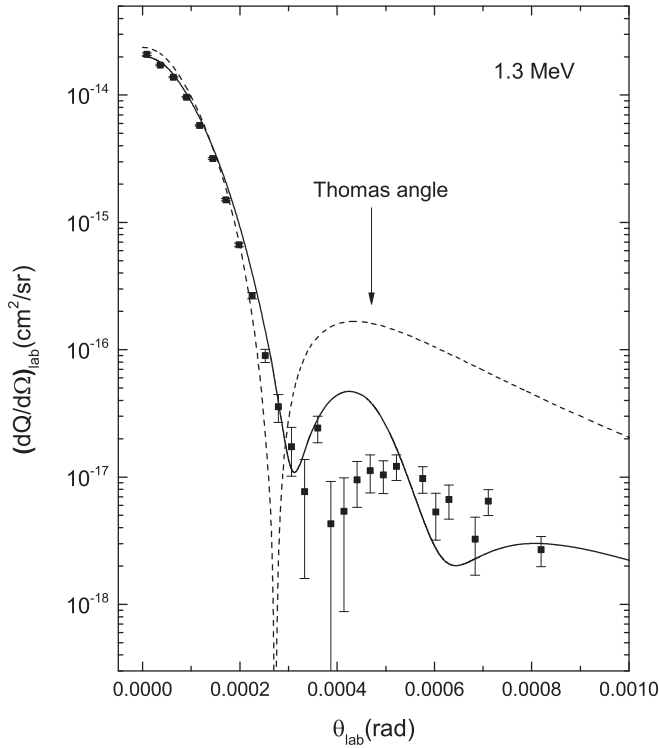


FIG. 6. Differential cross sections as a function of scattering angle  $\theta \equiv \theta_{\text{lab}}$  (rad) in the laboratory frame of reference at incident energy  $E = 1.3$  MeV for single-electron capture by protons from  $\text{He}(1s^2)$ . The solid curve represents the theoretical results obtained by using the prior BCIS-4B method (present computations). The dashed curve represents the theoretical results of the prior CB1-4B method (present computations). The initial ground state of atom  $\text{He}(1s^2)$  is described by means of the two-parameter wave function of Silverman *et al.* [44]. The explicit computations are carried out only for the ground state of  $\text{H}(1s)$  and the Oppenheimer  $n^{-3}$  scaling law with the multiplying factor 1.202 is used for  $\text{H}(n)$  to estimate the contribution from the whole spectrum of the excited states. Experimental data: ● Fischer *et al.* [14].

as predicted by the BCIS-4B method, is clearly visible in Figs. 6–10, as also summarized in Fig. 11. It is seen in Fig. 11 that the intensity of the Thomas peak increases with augmentation of the projectile velocity. It is then expected, in the case of nonradiative transitions, that at still higher incident velocities (not shown), the Thomas peak will yield the dominant contribution to single-electron capture cross sections. In general, and at least in the high-energy limit, all the second-order methods are anticipated to predict that the dip and the Thomas peak should be located at 0.28 and 0.47 mrad, respectively.

Horsdal-Pedersen *et al.* [60] experimentally detected the Thomas peak for electron capture from helium by protons using single-pass measurements by sweeping directly through the projectile scattering angles. This is a type of “counts per channel” measurement. Counts are the events associated with the generated hydrogen atoms that hit a detector at fixed scattering angles. Each scattering angle represents a channel in the measurement. As such, counts per channel are proportional to dimensionless differential cross sections taken as a function

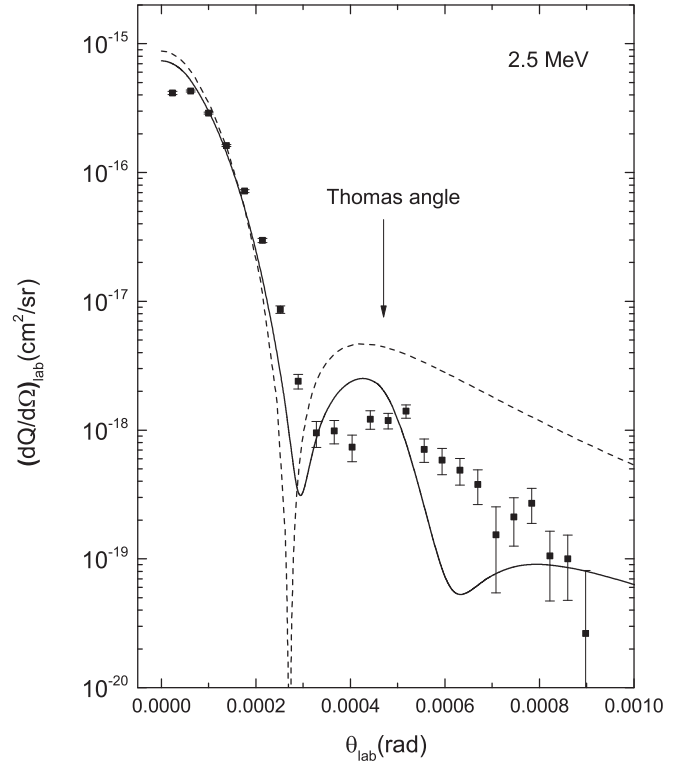


FIG. 7. The same as in Fig. 6, except for the incident energy of 2.5 MeV.

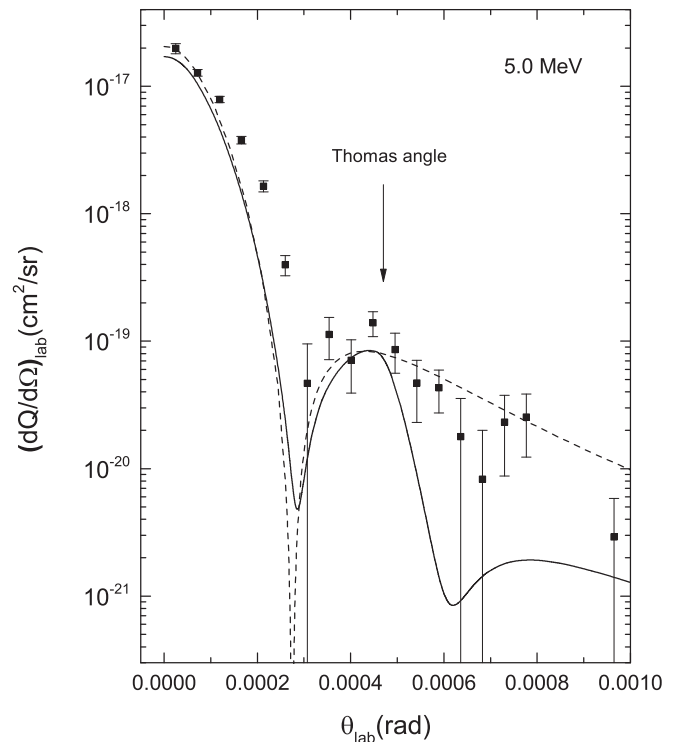


FIG. 8. The same as in Fig. 6, except for the incident energy of 5.0 MeV.

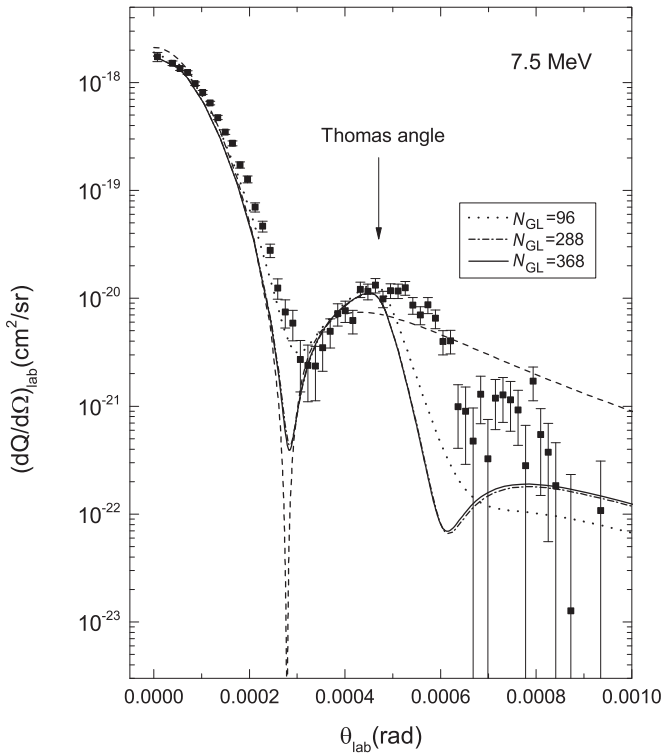


FIG. 9. The same as in Fig. 6, except for the incident energy of 7.5 MeV. The additional dotted and dot-dashed curves represent the results from the prior BCIS-4B method obtained using the two-dimensional Gauss-Legendre numerical integrations with 96 and 288 quadrature points per axis, respectively.

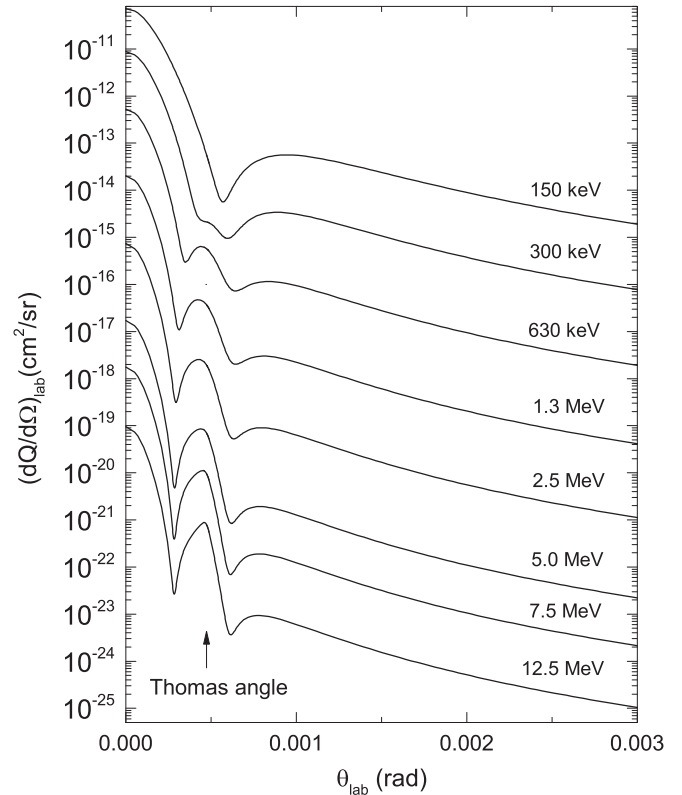


FIG. 11. Differential cross sections for single-electron capture by protons from  $\text{He}(1s^2)$  as a function of scattering angles at different incident energies. The curves represent the theoretical results obtained by using the prior BCIS-4B method (present computation).

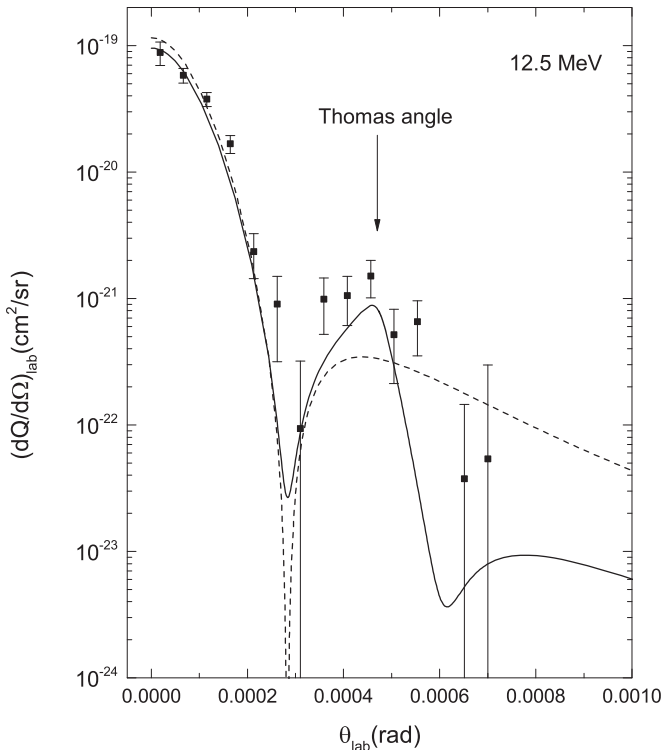


FIG. 10. The same as in Fig. 6, except for the incident energy of 12.5 MeV.

of scattering angles. The subsequent multiplication of these latter observables by a constant of proportionality, relating the output and input flux of particles per unit of surface, yields differential cross sections in units of area per steradian.

Decades later [12,14,15], also for the  $p$ -He collisions, the Thomas peak was recorded by multipass experiments that measure the momenta of recoiled ions. This was the COLTRIMS technique implemented within ion storage ring accelerators equipped with electron cooling. In such measurements, momentum and energy conservation laws are exploited to arrive at the differential cross sections as a function of scattering angles. Ion recoil momenta are very small (of the order of atomic units of momentum) and, thus, their measurements, being extremely difficult, necessitate cooling of both the target and projectiles. Projectiles are cooled by cold electron beams immersed into the ring from the electron gun in a direction parallel to the incident beam. This is done within a very small part of the path of the circulating hot projectiles. Cold cathode-produced electrons are adiabatically expanded prior to injection into the ring. Subsequently, these electrons are diverted from the primary beam away from the ring. In the said short overlapping part (about 1 m out of typically 50 m of the circumference of the ring), the parallel projectile and electron beams exchange their temperatures from hot to cold as dictated by the kinetic theory of gases. In this way, electrons become warmer and, as such, are diverted from projectiles. Simultaneously, projectiles become cooler,

as observed through monitoring the Schottky signal showing a much narrower beam profile (a Gaussian) of the incident beam. Here, hot and cold particle beams are the spread-out and narrow beams, respectively. This is clear from the fact that the beamwidth  $\Delta v$  in the Boltzmann distribution of the incident velocities  $v$  is proportional to the “gas” temperature  $T$  (here, a particle beam is referred to as particle “gas”). This is how the kinetic theory of gases is advantageously used for the primary beam collimation. This replaces the old-fashioned collimation achieved by making the projectiles pass through a sequence of well-aligned small holes in several parallel diaphragms. The target, on the other hand, is cooled by cryogenic molecular pumps. Overall, the purpose of projectile cooling is to collimate the stream of incident particles to a very narrow beam directed at the target. The goal of target cooling is to reduce the Brownian random motion in the target. With such a synergistic double cooling effect, the COLTRIMS technique is able to dramatically increase the angular resolution in measurements of differential cross sections and, thus, to peer into the collisional dynamics in an unprecedented way, as if it were a kind of a “reaction microscope” as noted earlier.

In Fig. 9, the three curves resulting from the BCIS-4B method are displayed at the impact proton energy of 7.5 MeV. They are obtained by employing three different sets of Gauss-Legendre quadratures with  $N_{GL} = 96$ , 288, and 368, where  $N_{GL}$  is the number of integration points. As can be seen from this figure, the results with  $N_{GL} = 96$  have not converged. However, convergence is achieved with  $N_{GL} = 288$  and persisted with  $N_{GL} = 368$ , in the sense that the angular distributions for these latter two sets are of practically indistinguishable shapes (moreover, a quantitative agreement between the full and dot-dashed curves is also seen with a slight difference appearing only above 0.6 mrad). The importance of this convergence test is best appreciated by observing that the Thomas peak is completely absent from the nonconverged angular distribution ( $N_{GL} = 96$ ). In fact, the set of 96 integration points, although itself quite large, is still insufficient to exhibit the double structure after the first dip around 0.28 mrad. For  $N_{GL} = 96$  the constructive interference prevails over the destructive ones, such that this double structure is washed out and, as a result, a flattened curve emerges after the dark angle.

With increasing projectile energy, the dark angle positions slowly move to the asymptotic scattering angle of the dip (0.28 mrad). Thus, at 12.5 MeV, both the CB1-4B and BCIS-4B methods show the same location of the dark angle at 0.28 mrad, as can be seen from Fig. 10. Of course, no Thomas peak is detected by the CB1-4B method which, as the first-order approximation, neglects the intermediate-continuum state of the active electron.

Many studies on ion-atom collisions concluded that the Thomas peak should appear exclusively at asymptotically high impact energies. This is not the case at all in the BCIS-4B method, which predicts the Thomas peak at both intermediate and high impact energies. For example, even at 300 keV, there is a hint of this double-scattering effect appearing as a left-sided shoulder of the Thomas peak lying within the dip (Fig. 3). Further, already at 630 keV, the Thomas peak becomes clearly visible and thereafter, with every increase of the impact energy, the Thomas peak becomes more pronounced (Fig. 11).

At intermediate impact energies (100, 150 keV), the dips in the BCIS-4B method occur at larger angles (at about 0.53 mrad) than in the case of the CB1-4B method, where they appear at about 0.48 mrad (Figs. 3 and 4). Interestingly, and by serendipity, the dark angles in the CB1-4B method at 100 and 150 keV are very close to the Thomas angle  $\theta_{lab} = 0.47$  mrad.

In both the BCIS-4B and CB1-4B methods, with augmentation of the impact energy, two simultaneous tendencies exist consisting of decrease of two dark angles and decrease of their difference (Figs. 4–10). Eventually, at sufficiently high impact energy, the BCIS-4B and CB1-4B method predict the same dark angle at 0.28 mrad (Figs. 9 and 10). At high energies the shapes of the angular distributions are completely different in the BCIS-4B and CB1-4B methods. At these energies, in the CB1-4B method, the dip is around 0.28 mrad and is followed by a broad and diffused maximum and a tail due to the internuclear Rutherford collision taking place at larger scattering angles. This latter peak will be hereafter called the broadband peak whose position converges to 0.48 mrad. The broadband and the Thomas peak should not be confused with each other. Despite being located at approximately the same scattering angle at high energies, the broadband peak in the CB1-4B method is not a second-order effect, which is a double scattering, billiard-type collision ( $Z_P - e_1 - Z_T$ ). Moreover, this broadband peak in the CB1-4B method diminishes with increasing energies relative to the forward peak. This latter trend is opposite to the increase of the Thomas peak height with respect to the forward peak at high impact energies in the BCIS-4B method. Further, at intermediate energies, the heights of the broadband peaks in the CB1-4B method are larger than those from the Thomas peaks in the BCIS-4B method with the opposite pattern at high energies. Also with increasing energies, the widths of the Thomas peaks in the BCIS-4B method become smaller as opposed to widening of the broadband peak in the CB1-4B method at higher energies.

In the BCIS-4B method, the dip at the dark angle (0.28 mrad) is followed by a more involved structure than in the CB1-4B method. Here, for all energies, at about 0.8 mrad, there is also a broadband peak and the adjacent tail stemming from the Rutherford scattering (Figs. 6–11). Additionally, in between the first dip at the dark angle (0.28 mrad), there is the Thomas peak at about 0.47 mrad. Finally, the Thomas and the broadband peak are separated by the second dip at about 0.61 mrad for all high energies (Fig. 11). The double-scattering peak at 0.47 mrad for the Thomas process  $Z_P - e_1 - Z_T$  is systematically much stronger than the broadband peak at 0.8 mrad. In the BCIS-4B method there are two peak-to-dip ratios that change with the increasing energy, one associated with the Thomas peak (0.47 mrad) and the other corresponding to the broadband peak (0.8 mrad).

The broadband peak in the BCIS-4B method is, in fact, an envelope of the angular distributions due to the three components representing the contributions from three different potentials  $2Z_P/R$ ,  $-Z_P/s_1$ , and  $-Z_P/s_2$  in the total perturbation  $V_1^d = 2Z_P/R - Z_P/s_1 - Z_P/s_2$  from (10). The first component due to repulsive potential ( $2Z_P/R$ ) describes the Rutherford scattering with no peak structure at any energy within the displayed angles on Figs. 12 and 13 at 150 keV and 7.5 MeV, respectively. On the other hand, at high energies, the second component stemming from the attractive potential

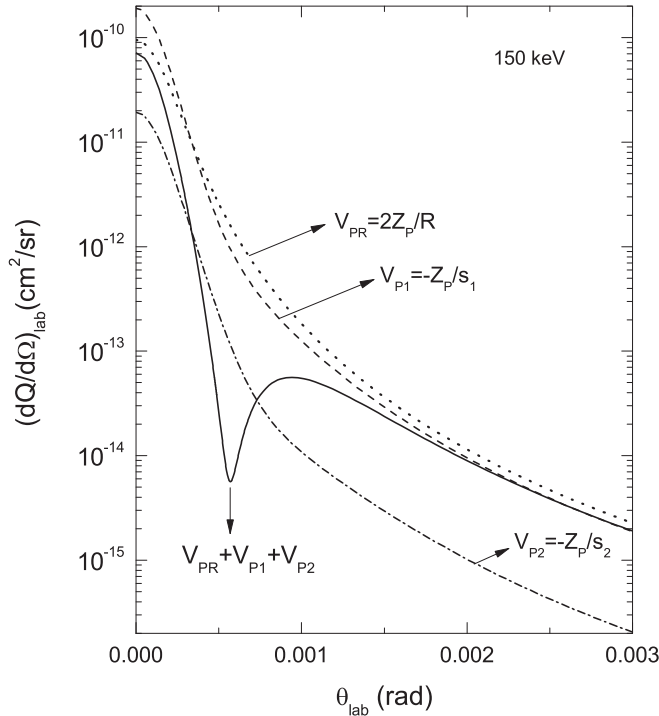


FIG. 12. Separate contributions from three different potentials in the complete perturbation  $V_i^d$  in the prior BCIS method at the incident energy 150 keV (present computation): dashed curve ( $V_{P1} = -Z_P/s_1$ ), dash-dotted curve ( $V_{P2} = -Z_P/s_2$ ), dotted curve ( $V_{PR} = 2Z_P/R$ ), and solid curve ( $V_i^d = V_{PR} + V_{P1} + V_{P2} = 2Z_P/R - Z_P/s_1 - Z_P/s_2$ ).

( $-Z_P/s_2$ ) has a well-delineated Thomas peak located at 0.47 mrad (Fig. 13). This is the earlier described Thomas process  $Z_P - e_1^S - e_2^S$ , which involves the static correlations of the electrons in the target wave function. According to Fig. 13, the ratio of the order of about  $10^{-4}$  of the heights of the two Thomas peaks (dash-dotted curve:  $Z_P - e_1^S - e_2^S$  and dashed curve:  $Z_P - e_1 - Z_T$ ) points to the relative weakness of the static correlations in helium. The peak for the Thomas process  $Z_P - e_1 - Z_T$  (dashed curve in Fig. 13), up to the level of the first dip, is a perfectly symmetric Lorentzian. However, the Thomas peak in the solid line which includes the three potentials via  $V_i^d$  is asymmetric with a shoulder on the left-hand side. This is due to the constructive interference between the contributions from  $V_{P1} = -Z_P/s_1$  and  $V_{PR} = 2Z_P/R$  in  $V_i^d$  (the Thomas peak associated with  $V_{P2} = -Z_P/s_2$  is too weak to participate in this interference). Notice that in the post version of the CDW-4B method for process (45), the two peaks for the Thomas processes  $Z_P - e_1 - Z_T$  and  $Z_P - e_1 - e_2$  are of practically the same height [2,6]. In this latter method the dynamic correlations are explicitly included in the post transition amplitude by way of the perturbation  $V_f$  from (3), which contains the electronic repulsion  $1/r_{12}$ .

As stated, in contradistinction with the CBI-4B method, there are two dips in the differential cross sections from the BCIS-4B method. Figure 13 at 7.5 MeV is a particularly clear illustration of the origin of these two dips. Therein, it is seen that the curves due to  $-Z_P/s_1$  and  $2Z_P/R$  cross each other twice, precisely at the positions of the two dips (0.28 and

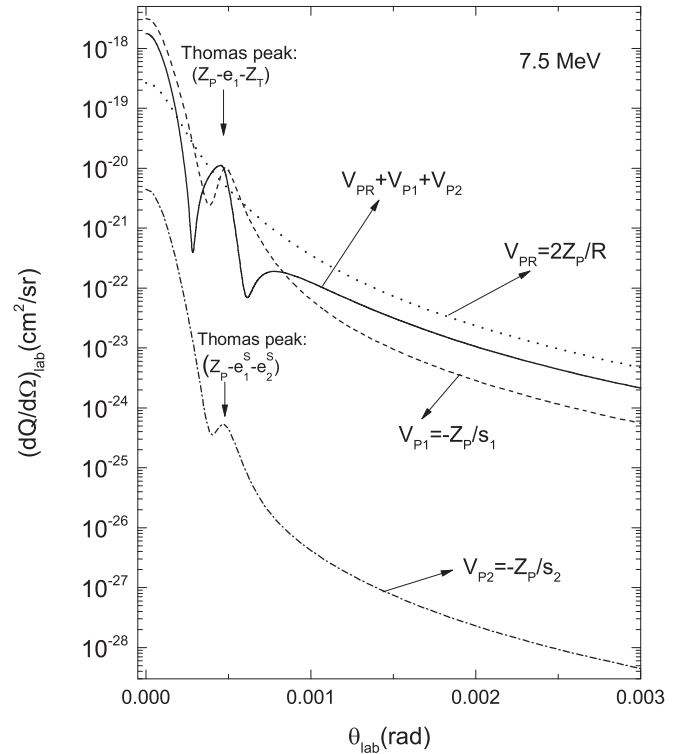


FIG. 13. Separate contributions from three different potentials in the complete perturbation  $V_i^d$  in the prior BCIS method at the incident energy 7.5 MeV (present computation): dashed curve ( $V_{P1} = -Z_P/s_1$ ), dash-dotted curve ( $V_{P2} = -Z_P/s_2$ ), dotted curve ( $V_{PR} = 2Z_P/R$ ), and solid curve ( $V_i^d = V_{PR} + V_{P1} + V_{P2} = 2Z_P/R - Z_P/s_1 - Z_P/s_2$ ). The upper Thomas peak (dashed line) at the critical angle 0.47 mrad is due to the usual distorted-wave quantum-mechanical counterpart of the classical Thomas billiard-type double scattering  $Z_P - e_1 - Z_T$ . The lower Thomas peak (dot-dashed line) at the same Thomas critical angle 0.47 mrad stems from the static-correlation-induced double scattering-type event  $Z_P - e_1^S - e_2^S$ , involving the projectile, the active (to be captured) and the passive (noncaptured) electrons. Here, superscript  $S$ , standing for static correlations, is used for the electrons to avoid confusing  $Z_P - e_1^S - e_2^S$  with  $Z_P - e_1 - e_2$ , which explicitly invokes the electron-electron repulsion  $1/r_{12}$  via the perturbation potential  $V_f$  in (3) from the post BCIS-4B method. The Thomas process  $Z_P - e_1 - e_2$  is absent from the prior BCIS-4B method, since  $V_i$  from (3) and its eikonal approximation  $V_i^d$  in (10) do not have  $1/r_{12}$ .

0.61 mrad). Thus, in the close vicinity of scattering angles 0.28 and 0.61 mrad, both dips result from destructive interference of these two contributions of different signs  $-Z_P/s_1$  and  $2Z_P/R$  in the transition amplitude (25). Hence, in this angular region, the contribution from  $-Z_P/s_2$ , although relatively small, is still able to dominate the yield due to the difference  $2Z_P/R - Z_P/s_1$  in  $V_i^d$  from (25). The contribution from  $-Z_P/s_1$  has its own dip at 0.38 mrad. This is not due to any cancellation with another potential, but rather to a destructive interference of various wavelets from the Coulomb function. The dip at 0.38 mrad is partially filled by the contribution from  $2Z_P/R$ , which also shifts the dip at 0.38 to 0.28 mrad, which is the final position of the dip in the solid line from  $V_i^d$ .

Figure 12 at 150 keV displays an entirely different situation. Therein, there are no Thomas peaks at all and only one dip shows up at 0.61 mrad. With the exception of the forward peak, none of the three component curves that are due to  $-Z_P/s_1$ ,  $-Z_P/s_2$ , and  $2Z_P/R$  exhibit any other structure. Rather these differential cross sections show a systematic trend of continuously decreasing functions of scattering angles. Here, the curves due to  $-Z_P/s_1$  and  $2Z_P/R$  cross each other only once and this is around 0.28 mrad. This does not lead to a dip, which is shifted to 0.61 mrad. The lack of destructive interference between the contributions from  $-Z_P/s_1$  and  $2Z_P/R$  is explained by a significant yield from  $-Z_P/s_2$  (which was totally negligible at 7.5 MeV in Fig. 13). At the dip near 0.61 mrad, there is no crossing of the curves arising from  $-Z_P/s_1$  and  $2Z_P/R$ . Nevertheless, the dip at 0.61 mrad still appears, and this is due to a near compensation of the contribution from  $2Z_P/R$  and the difference  $-Z_P/s_1 - Z_P/s_2$  (again, here too, the yield from  $-Z_P/s_2$  is significant).

A further inspection of these two latter figures also identifies the origin of the broadband peak after the first and second dip in Figs. 12 and 13, respectively. The broadband peak is due to the different rates of decrease of the contributions from  $-Z_P/s_1$ ,  $-Z_P/s_2$ , and  $2Z_P/R$ . With augmentation of the scattering angles, the differential cross sections due to  $-Z_P/s_2$  fall off faster than those from  $-Z_P/s_1$  and  $2Z_P/R$ , as seen in Figs. 12 and 13. Additionally, the wavelets from the Coulomb function centered at  $Z_T - 1$  can also influence the overall interference pattern. At intermediate energies, this is evidenced by shifting (towards larger scattering angles) of the dip predicted by the BCIS-4B method relative to the dip from the CB1-4B method (Fig. 4).

#### D. Influence of excited hydrogen states at intermediate and high energies

We have found that sharp minima in the differential cross sections from the CB1-4B method can be partially filled by inclusion of the excited states of the atomic hydrogen. A similar effect has previously been reported in Ref. [61] in the case of single-electron capture treated within the three-body boundary-corrected first Born (CB1-3B) method. As an illustration of this effect within the CB1-4B method, the computations of the state-selective cross sections for the  $p - \text{He}$  collisions are performed at 100 keV and 7.5 MeV. The obtained results are shown in Figs. 14 and 15, respectively. This effect is more pronounced at 100 keV than at 7.5 MeV, implying that the contributions from electron capture into the excited state are more important at lower than at higher impact energies.

Differential cross sections  $(dQ/d\Omega)_{\text{tot}}$  for capture summed over all the final states of atomic hydrogen according to the Oppenheimer scaling law [50,51] can be written as

$$\left(\frac{dQ}{d\Omega}\right)_{\text{tot}} = \sum_{n=1}^4 \gamma_n \left(\frac{dQ}{d\Omega}\right)_n \quad (n \equiv n_{f_1}, l \equiv l_{f_1}, m \equiv m_{f_1}), \quad (46)$$

where  $(dQ/d\Omega)_n = \sum_{l=0}^{n-1} (dQ/d\Omega)_{nl}$ ,  $(dQ/d\Omega)_{nl} = \sum_{m=-l}^{+l} (dQ/d\Omega)_{nlm}$  with  $\gamma_n = 1$  ( $n = 1, 2, 3$ ) and  $\gamma_4 = 2.561$ . Here,

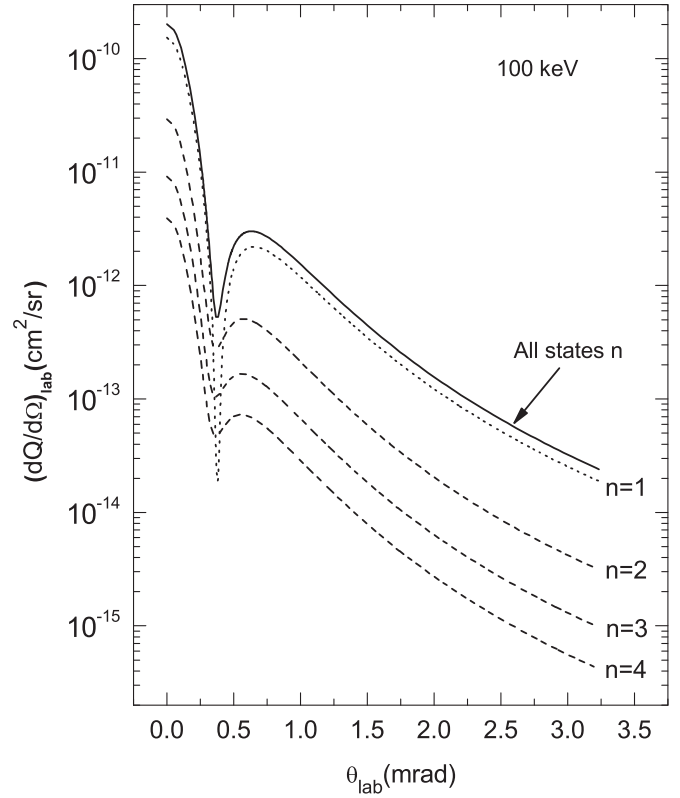


FIG. 14. Differential state-selective cross sections for electron capture by protons from  $\text{He}(1s^2)$  at the proton energy of 100 keV. The curves represent the theoretical results obtained using the prior CB1-4B method (present computations) for different principal quantum number  $n$  of the captured electron in the final channel.

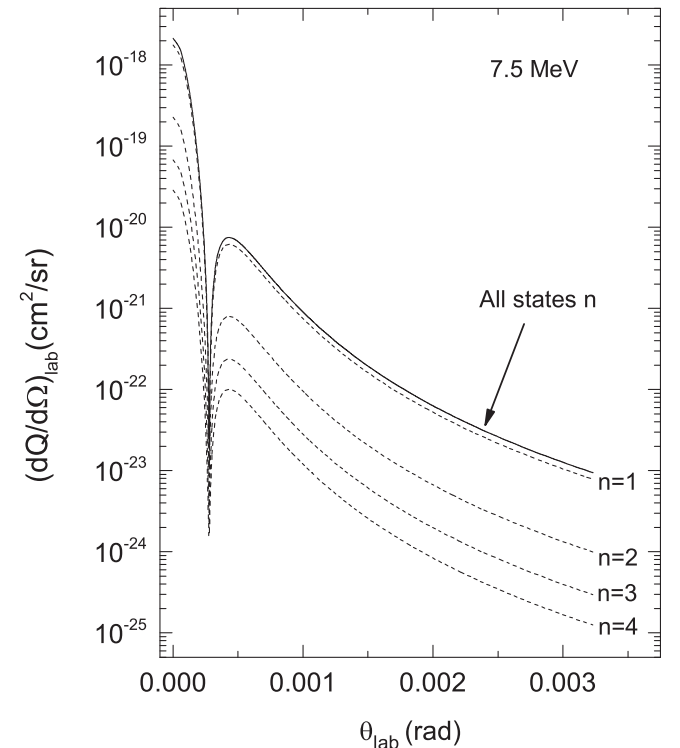


FIG. 15. The same as in Fig. 14, except for the incident energy of 7.5 MeV.

the numerical factor 2.561 comes from the Oppenheimer  $n^{-3}$  scaling law which takes approximately into account the contributions from all the levels with  $n \geq 5$  (Appendix B). In practice, we found that for the  $p - \text{He}$  collisions, the inclusion of the higher partial cross sections  $(dQ/d\Omega)_{n=5}$  and beyond does not influence the results for  $(dQ/d\Omega)_{\text{tot}}$ . The latter results explicitly take into account the exact contributions from the  $n \leq 4$  states, whereas the yield from the higher excited states ( $n \geq 5$ ) is included approximately by the Oppenheimer scaling rule. As can be seen from Figs. 14 and 15, the ground-state transfer is the dominant channel over electron capture to excited states.

#### IV. CONCLUSIONS

We have investigated the role of the intermediate ionization continua in the problem of one-electron capture from two-electron atomic systems by completely stripped projectiles at intermediate and high impact energies. The analysis is carried out by means of the four-body boundary-corrected continuum-intermediate-state (BCIS-4B) approximation. The total scattering wave functions of the BCIS-4B theory satisfy the proper boundary conditions in both the entrance and exit channels. In addition to the long-range Coulomb distortions of the plane waves for the relative motion of the two charged aggregates, the BCIS-4B method accounts for the intermediate ionization continua of the captured electron in the exit channel. Detailed comparisons are made between the results from this second-order method and the four-body boundary-corrected first Born (CB1-4B) approximation. The latter method ignores the continuum-intermediate states of the electron and includes only the logarithmic Coulomb phase distortions due to the relative motion of heavy particles. The outcome of these comparisons provides direct evidence that full Coulomb electronic continuum-intermediate states of the captured electron play an important role for single charge exchange. We have carried out an analytical reduction of the original nine-dimensional integral for the transition amplitude to a straightforward and efficient two-dimensional numerical quadrature over the real variables. A general program is written based upon the obtained semianalytical expression for the arbitrary nuclear charges of the bare projectile and heliumlike targets. This program is presently used to compute differential and total cross sections for single-electron capture in  $p - \text{He}$  collisions.

The obtained theoretical results for differential cross sections are compared with the related experimental data that are available at several intermediate energies 100, 150, and 300 keV, as well as at higher energies 1.3, 2.5, 5.0, 7.5, and 12.5 MeV. The results from the BCIS-4B method are in overall good agreement with the existing experimental data. In particular, in the narrow forward cone, the agreement between the BCIS-4B theory and the experiment is excellent. Theory and experiments do not agree around the so-called dark angle, as manifested via a dip, which comes from a destructive interference of the parts of the amplitudes corresponding to the attractive and repulsive Coulomb potentials.

By increasing the impact energy, the BCIS-4B method clearly shows the two Thomas peaks both located precisely

at the same scattering angle  $\theta_{\text{lab}} = 0.47$  mrad. One of them is the usual double scattering involving the two nuclei and the active electron (the electron to be captured by the projectile). The other corresponds to capture of the active electron by the interaction of the projectile nucleus and the nontransferred electron (the electron to remain bound to the target nucleus after the collision). This latter mechanism for capture is assisted by the static correlations between the two electrons in the target wave function rather than stemming from the usual billiard-type Thomas double scattering. The height of the Thomas peak with the captured electron is much stronger than that of the Thomas peak involving the noncaptured electron in the case of the presently employed two-parameter ground-state helium wave function with radial static correlations alone. The Thomas peak with the nontransferred electron may become more intense if both radial and angular static correlations of the electrons are included in the helium wave function.

For scattering angles above the dark angle, the CB1-4B approximation systematically and largely overestimates the experimental data. Significant difference between the results of the CB1-4B and BCIS-4B methods at this angular region can be directly attributed to the importance of the full Coulomb electronic continuum-intermediate states of the captured electron. It is also shown by way of the CB1-4B approximation that the contribution from the excited states of the atomic hydrogen in the  $p - \text{He}$  collisions can partially fill in the unphysical and experimentally unobserved extremely sharp dip. Although not accomplished in the current study, a similar partial filling in of the dip is expected in the BCIS-4B method, provided that the contribution from the excited states of the atomic hydrogen is taken into account.

The computed total cross sections in the BCIS-4B method for the investigated one-electron capture in the  $p - \text{He}$  collisions are found to be in excellent agreement with the available experimental data above 50 keV. These cross sections vary within 11 orders of magnitude for impact energies covering three orders of magnitude. Overall, the present thorough analysis shows that the BCIS-4B theory can confidently be further explored for many other collisional systems involving single-electron capture for important and versatile applications both in basic and applied physics (thermonuclear fusion energy research, hadrontherapy, etc.).

#### ACKNOWLEDGMENTS

I.M. and N.M. thank the Ministry of Education, Science and Technological Development of the Republic of Serbia for support through Project No. 171020. D.Ž.B. appreciates support by the Research Funds of the Swedish Cancer Society (Cancerfonden), the Karolinska University Hospital's Radiumhemmet, the City Council of Stockholm (FoUU), and the Karolinska Institute. The authors would like to express their gratitude to Dr. H. Schmidt and Dr. X. Ma for providing the tabular forms of their experimental data on electron capture from helium by protons.

## APPENDIX A

The quantity  $\mathcal{A}_k$  appearing in Eq. (33) from the main text is given by

$$\mathcal{A}_k = \int d\vec{s}_1 e^{-i\vec{v}\cdot\vec{s}_1} \Psi_k(\vec{x}_1) \varphi_P^*(\vec{s}_1) = \int d\vec{s}_1 e^{-i\vec{v}\cdot\vec{s}_1} \varphi_P^*(\vec{s}_1) \left[ \int d\vec{q} e^{-i\vec{q}\cdot\vec{x}_1} \tilde{\Psi}_k(\vec{q}) \right], \quad (\text{A1})$$

where  $\tilde{\Psi}_k(\vec{q}) = \mu_1 / [\pi^2 (|\vec{q} + \vec{v}\tau|^2 + \mu_1^2)^2]$  is the Fourier transform of  $\Psi_k(\vec{x}_1)$  with  $\mu_1 = \alpha_k - i v \tau$ . Further,  $\mathcal{A}_k$  can be analytically transformed to the following form:

$$\begin{aligned} \mathcal{A}_k &= 8\mu_1 \sqrt{\frac{Z_P^5}{\pi^3}} e^{-i\vec{\beta}\cdot\vec{R}} \int d\vec{q} \frac{e^{-i\vec{q}\cdot\vec{R}}}{(|\vec{q} - \vec{\alpha}|^2 + Z_P^2)(|\vec{q} + \vec{\beta}_1|^2 + \mu_1^2)^2} \\ &= 48\mu_1 \sqrt{\frac{Z_P^5}{\pi^3}} e^{-i\vec{\beta}\cdot\vec{R}} \int_0^1 dt t(1-t) \int d\vec{q} \frac{e^{-i\vec{q}\cdot\vec{R}}}{(|\vec{q} - \vec{Q}_1|^2 + \Delta_1^2)^4} \\ \therefore \mathcal{A}_k &= 2\mu_1 \sqrt{Z_P^5 \pi} e^{-i\vec{\beta}\cdot\vec{R}} \int_0^1 dt \frac{t(1-t)}{\Delta_1^5} (3 + 3\Delta_1 R + \Delta_1^2 R^2) e^{-i\vec{Q}_1\cdot\vec{R} - \Delta_1 R}, \end{aligned} \quad (\text{A2})$$

where  $\Delta_1^2 = v_1^2 t(1-t) + Z_P^2 t + \mu_1^2(1-t)$ ,  $\vec{\beta}_1 = \vec{\beta} + \vec{v}\tau$ ,  $\vec{v}_1 = \vec{v}(1-\tau)$ , and  $\vec{Q}_1 = \vec{\alpha} - \vec{\beta}_1(1-t)$ . Here, the well-known Feynman identity [62] is also utilized. Applying the technique analogous to the one just outlined for  $\mathcal{A}_k$ , the quantity  $\mathcal{B}_k$  from Eq. (33) becomes

$$\begin{aligned} \mathcal{B}_k &= \int d\vec{s}_1 e^{-i\vec{v}\cdot\vec{s}_1} \frac{\varphi_P^*(\vec{s}_1)}{s_1} \Psi_k(\vec{x}_1) \\ &= \int d\vec{s}_1 e^{-i\vec{v}\cdot\vec{s}_1} \frac{\varphi_P^*(\vec{s}_1)}{s_1} \left[ \int d\vec{q} e^{-i\vec{q}\cdot\vec{x}_1} \tilde{\Psi}_k(\vec{q}) \right] \\ &= 4\mu_1 \sqrt{\frac{Z_P^3}{\pi^3}} e^{-i\vec{\beta}\cdot\vec{R}} \int d\vec{q} \frac{e^{-i\vec{q}\cdot\vec{R}}}{(|\vec{q} - \vec{\alpha}|^2 + Z_P^2)(|\vec{q} + \vec{\beta}_1|^2 + \mu_1^2)^2} \\ &= 8\mu_1 \sqrt{\frac{Z_P^3}{\pi^3}} e^{-i\vec{\beta}\cdot\vec{R}} \int_0^1 dt (1-t) \int d\vec{q} \frac{e^{-i\vec{q}\cdot\vec{R}}}{(|\vec{q} - \vec{Q}_1|^2 + \Delta_1^2)^3}, \\ \therefore \mathcal{B}_k &= 2\mu_1 \sqrt{Z_P^3 \pi} e^{-i\vec{\beta}\cdot\vec{R}} \int_0^1 dt \frac{(1-t)}{\Delta_1^3} (1 + \Delta_1 R) e^{-i\vec{Q}_1\cdot\vec{R} - \Delta_1 R}. \end{aligned} \quad (\text{A3})$$

A similar calculation can also be carried out for  $\mathcal{D}_l$  with the intermediate expression

$$\begin{aligned} \mathcal{D}_l &= \int d\vec{s}_2 \varphi_T^*(\vec{x}_2) e^{-\alpha_l x_2} \frac{1}{s_2} \\ &= 2\zeta \sqrt{\pi Z_T^3} \int_0^1 dt_1 \frac{1-t_1}{\Delta_2^3} (1 + \Delta_2 R) e^{-\Delta_2 R}, \end{aligned} \quad (\text{A4})$$

where  $\zeta = Z_T + \alpha_l$  and  $\Delta_2 = \zeta \sqrt{1-t_1}$ . Moreover, the remaining integral in  $\mathcal{D}_l$  can be analytically calculated yielding

$$\mathcal{D}_l = 2 \frac{\sqrt{\pi Z_T^3}}{\zeta^2} \left[ \frac{4}{\zeta R} - 2e^{-\zeta R} \left( 1 + \frac{2}{\zeta R} \right) \right]. \quad (\text{A5})$$

It should be noted that the same integral  $\mathcal{D}_l$  also appears in the CB1-4B calculation. Such a derivation of the closed form for the integral  $\mathcal{D}_l$  provides a reduction of the original nine-dimensional integral of the prior CB1-4B transition amplitude [35] to a one-dimensional quadrature. Finally, a closed form can likewise be derived for the integral  $\mathcal{C}_l$  from Eq. (33) and the result is

$$\mathcal{C}_l = \int d\vec{s}_2 \varphi_T^*(\vec{x}_2) e^{-\alpha_l x_2} = \sqrt{\frac{Z_T^3}{\pi}} \frac{8\pi}{(Z_T + \alpha_l)^3}. \quad (\text{A6})$$

In this way, the quantity  $\mathcal{S}_{\text{if}}$  from Eq. (30) in the main text becomes

$$\begin{aligned} \frac{\mathcal{S}_{\text{if}}(\tau)}{4\pi Z_P^{5/2} Z_T^{3/2}} &= \sum_{k,l} N_{\alpha_k} N_{\alpha_l} \frac{\mu_1}{\zeta^3} \int_0^1 dt \frac{1-t}{\Delta_1^3} \{ 12p I_0^{(\Delta_1)} + 4(3p\Delta_1 - 1) I_1^{(\Delta_1)} + 4\Delta_1(p\Delta_1 - 1) I_2^{(\Delta_1)} \\ &\quad + p[12I_0^{(\Delta)} + 6(\zeta + 2\Delta_1) I_1^{(\Delta)} + 2\Delta_1(3\zeta + 2\Delta_1) I_2^{(\Delta)} + 2\zeta \Delta_1^2 I_3^{(\Delta)}] \}, \end{aligned} \quad (\text{A7})$$

where  $p = Z_{\text{PT}}/\Delta_1^2$ . The quantities  $I_{0,1,2}^{(\Delta_1)}$  and  $I_{0,1,2,3}^{(\Delta)}$  are defined by the remaining integral:

$$I_n^{(\lambda)} = \int d\vec{R} R^{n-1} e^{-i\vec{Q}_1\cdot\vec{R} - \lambda R} (vR + \vec{v}\cdot\vec{R})^{i\xi}, \quad (\lambda = \Delta_1, \Delta). \quad (\text{A8})$$

The integrals from (A8) for  $0 \leq n \leq 4$  have been calculated by Belkić [63] and the analytical results are given by the following concise expressions:

$$I_0^{(\lambda)} = 4\pi\Gamma(1+i\xi)\mathcal{F}^{(\lambda)}, \quad (\text{A9})$$

$$I_1^{(\lambda)} = 8\pi\Gamma(1+i\xi)D^{(\lambda)}\mathcal{F}^{(\lambda)}[1-i\xi C^{(\lambda)}], \quad (\text{A10})$$

$$I_2^{(\lambda)} = -8\pi\Gamma(1+i\xi)\frac{D^{(\lambda)}\mathcal{F}^{(\lambda)}}{\lambda}[A_\alpha^{(\lambda)}+i\xi B_\alpha^{(\lambda)}], \quad (\text{A11})$$

$$I_3^{(\lambda)} = -16\pi\Gamma(1+i\xi)\frac{[D^{(\lambda)}]^2\mathcal{F}^{(\lambda)}}{\lambda}[A_\beta^{(\lambda)}+i\xi B_\beta^{(\lambda)}]. \quad (\text{A12})$$

The other quantities appearing in Eqs. (A9)–(A12) are

$$\mathcal{F}^{(\lambda)} = \frac{[B^{(\lambda)}]^{i\xi}}{Q_1^2 + \lambda^2}, \quad B^{(\lambda)} = \frac{2(v\lambda - i\vec{Q}_1 \cdot \vec{v})}{Q_1^2 + \lambda^2}, \quad (\text{A13})$$

$$C^{(\lambda)} = \frac{v}{\lambda B^{(\lambda)}} - 1, \quad A^{(\lambda)} = \frac{\lambda^2}{Q_1^2 + \lambda^2}, \quad D^{(\lambda)} = \frac{A^{(\lambda)}}{\lambda}, \quad (\text{A14})$$

$$A_\alpha^{(\lambda)} = 1 - 4A^{(\lambda)}, \quad B_\alpha^{(\lambda)} = 1 + 2A^{(\lambda)}C^{(\lambda)}, \quad (\text{A15})$$

$$C_\alpha^{(\lambda)} = C^{(\lambda)}[4 + (1 - i\xi)C^{(\lambda)}], \quad (\text{A16})$$

$$A_\beta^{(\lambda)} = 6(1 - 2A^{(\lambda)}), \quad B_\beta^{(\lambda)} = 2A^{(\lambda)}C_\beta^{(\lambda)} + 3D_\beta^{(\lambda)}, \quad (\text{A17})$$

$$C_\beta^{(\lambda)} = C^{(\lambda)}\{18 + 9(1 - i\xi)C^{(\lambda)} + (1 - i\xi)(2 - i\xi)[C^{(\lambda)}]^2\}, \quad (\text{A18})$$

$$D_\beta^{(\lambda)} = 2 - (1 + i\xi)C^{(\lambda)}. \quad (\text{A19})$$

Notice that in Ref. [64], the more general case of integral (A8), which additionally involves the spherical harmonics  $Y_{l,m}(\hat{\vec{R}})$ , has been considered and the analytical results were obtained for arbitrary triple  $\{n, l, m\}$ .

## APPENDIX B

At sufficiently high impact energies, in the first-order Oppenheimer-Brinkman-Kramers (OBK1) approximation [65] for electron capture from hydrogenlike atomic systems by bare nuclei, the total cross sections corresponding to two final states with different principal quantum numbers  $n$  and  $n'$  scale according to  $(n'/n)^3$ . We assume that the same Oppenheimer scaling also applies to the BCIS-4B method for electron capture via (1), i.e.,  $Z_P + (Z_T; e_1, e_2)_i \rightarrow (Z_P, e_1)_{nlm} + (Z_T, e_2)_{l'}$ . In such a case, high-energy total cross sections in the BCIS-4B method for electron capture into any final state with the principal quantum number  $n$  of the hydrogenlike atomic system  $(Z_P, e_1)_n$  summed over  $\{l, m\}$  can

be estimated by means of the Oppenheimer  $n^{-3}$  scaling law [50,51] as

$$\frac{Q_n}{Q_{n'}} \approx \left(\frac{n'}{n}\right)^3, \quad Q_n = \sum_{l=0}^{n-1} Q_{nl}, \quad Q_{nl} = \sum_{m=-l}^{+l} Q_{nlm}, \quad (\text{B1})$$

$$Q_{\text{tot}} = \sum_{n=1}^{N-1} Q_n + \gamma(3, N-1)Q_N, \quad (\text{B2})$$

$$\gamma(3, N) = 1 + (N+1)^3\zeta(3) - \sum_{n=1}^{N+1} \left(\frac{N+1}{n}\right)^3.$$

Here, there is a similar sum in  $Q_{n'}$  for all the degenerate levels at each fixed value of the principal quantum number  $n'$ . Quantity  $\zeta(s)$  in (B2) represents the Riemann  $\zeta$  function  $\zeta(s) = \sum_{n=1}^{\infty} n^{-s}$  with the specific value  $\zeta(3) \approx 1.202056903$  [66]. Parameter  $N$  in  $\gamma(3, N)$  is a positive integer which is chosen to coincide with the lowest value of  $n$  required for convergence of the sum over all the final bound states of the projectile.

In order to approximately take into account the contributions from all the levels  $n \geq 2$ , we should set  $N = 1$  and use the formula  $Q_{\text{tot}} \simeq Q(\Sigma_1) = \gamma(3, 0)Q_1 = \zeta(3)Q_1 \approx 1.202Q_1$ . This was used in computations of all the presently reported total cross sections. Similarly, to explicitly account for the states with  $n \leq 4$ , we should put  $N = 4$  and employ the expression  $Q_{\text{tot}} \simeq Q(\Sigma_4) = Q_1 + Q_2 + Q_3 + \gamma(3, 3)Q_4 \approx Q_1 + Q_2 + Q_3 + 2.561Q_4$ . Here, the number 2.561 modifies  $Q_4$  by allowing for the approximate contributions from all the levels  $n \geq 5$ , where  $\gamma(3, 3) = 64[\zeta(3) - 251/216] = 2.561274 \approx 2.561$ .

The same  $n^{-3}$  scaling law is supposed to be applicable to differential cross sections:

$$\left(\frac{dQ}{d\Omega}\right)_{\text{tot}} = \sum_{n=1}^{N-1} \left(\frac{dQ}{d\Omega}\right)_n + \gamma(3, N-1) \left(\frac{dQ}{d\Omega}\right)_N, \quad (\text{B3})$$

where  $(dQ/d\Omega)_n = \sum_{l=0}^{n-1} (dQ/d\Omega)_{nl}$  and  $(dQ/d\Omega)_{nl} = \sum_{m=-l}^{+l} (dQ/d\Omega)_{nlm}$ . All the differential and total cross sections  $dQ/d\Omega$  and  $Q$  from the BCIS-4B method in the main text are from the formulas  $(dQ/d\Omega)_{\text{tot}} \equiv dQ/d\Omega \approx 1.202(dQ/d\Omega)_1$  and  $Q_{\text{tot}} \equiv Q \approx 1.202Q_1$ . These formulas are also employed in the CB1-4B method for nearly all the differential and total cross sections from the main text. The only exceptions are Figs. 14 and 15 that display differential cross sections from the CB1-4B method computed for  $N = 4$  in the general expression (B3), which leads to the numerical factor  $\gamma_4 = 2.561$  in Eq. (46).

- [1] Dž. Belkić, R. Gayet, and A. Salin, *Phys. Rep.* **56**, 279 (1979).  
 [2] Dž. Belkić, I. Mančev, and J. Hanssen, *Rev. Mod. Phys.* **80**, 249 (2008).  
 [3] Dž. Belkić, *J. Math. Chem.* **47**, 1366 (2010).

- [4] Dž. Belkić, *J. Math. Chem.* **47**, 1420 (2010).  
 [5] Dž. Belkić, *Principles of Quantum Scattering Theory* (Institute of Physics, Bristol, 2004).  
 [6] Dž. Belkić, *Quantum Theory of High-Energy Ion-Atom Collisions* (Taylor & Francis, London, 2008).

- [7] Dž. Belkić, in *Fast Ion-Atom and Ion-Molecule Collisions*, edited by Dž. Belkić (World Scientific, Singapore, 2013), pp. v–xix.
- [8] Dž. Belkić, in *Theory of Heavy Ion Collision Physics in Hadron Therapy*, edited by Dž. Belkić, Special Issue, Adv. Quantum Chem. **65**, xiii–xv (2013).
- [9] R. Dörner, V. Mergel, O. Jagutzki, L. Spielberger, J. Ullrich, R. Moshhammer, and H. Schmidt-Böcking, *Phys. Rep.* **330**, 95 (2000).
- [10] V. Mergel, R. Dörner, Kh. Khayyat, M. Achler, T. Weber, O. Jagutzki, H. J. Ludde, C. L. Cocke, and H. Schmidt-Böcking, *Phys. Rev. Lett.* **86**, 2257 (2001).
- [11] J. Ullrich, R. Moshhammer, A. Dorn, R. Dörner, L. Ph. H. Schmidt, and H. Schmidt-Böcking, *Rep. Prog. Phys.* **66**, 1463 (2003).
- [12] D. Fischer, K. Stöckel, H. Cederquist, H. Zettergren, P. Reinhed, R. Schuch, A. Källberg, A. Simonsson, and H. T. Schmidt, *Phys. Rev. A* **73**, 052713 (2006).
- [13] M. S. Schöffler, J. Titze, L. Ph. H. Schmidt, T. Jahnke, N. Neumann, O. Jagutzki, H. Schmidt-Böcking, R. Dörner, and I. Mančev, *Phys. Rev. A* **79**, 064701 (2009).
- [14] D. Fischer, M. Gudmundsson, Z. Berényi, N. Haag, H. A. B. Johansson, D. Misra, P. Reinhed, A. Källberg, A. Simonsson, K. Stöckel, H. Cederquist, and H. T. Schmidt, *Phys. Rev. A* **81**, 012714 (2010).
- [15] M. Gudmundsson, D. Fischer, N. Haag, H. A. B. Johansson, D. Misra, P. Reinhed, H. Schmidt-Böcking, R. Schuch, M. Schöffler, K. Stöckel, H. T. Schmidt, and H. Cederquist, *J. Phys. B* **43**, 185209 (2010).
- [16] D. L. Guo, X. Ma, S. F. Zhang, X. L. Zhu, W. T. Feng, R. T. Zhang, B. Li, H. P. Liu, S. C. Yan, P. J. Zhang, and Q. Wang, *Phys. Rev. A* **86**, 052707 (2012).
- [17] H.-K. Kim, M. S. Schöffler, S. Houamer, O. Chuluunbaatar, J. N. Titze, L. Ph. H. Schmidt, T. Jahnke, H. Schmidt-Böcking, A. Galstyan, Yu. V. Popov, and R. Dörner, *Phys. Rev. A* **85**, 022707 (2012).
- [18] M. Alessi, S. Otronto, and P. Focke, in *Fast Ion-Atom and Ion-Molecule Collisions*, edited by Dž. Belkić (World Scientific, Singapore, 2013), pp. 27–53.
- [19] A. Igarashi, L. Gulyás, and A. Ohsaki, *Eur. Phys. J. D* **66**, 79 (2012).
- [20] I. Mančev, V. Mergel, and L. Schmidt, *J. Phys. B* **36**, 2733 (2003).
- [21] I. Mančev, *Europhys. Lett.* **69**, 200 (2005).
- [22] L. Gulyás, A. Igarashi, and T. Kirchner, *J. Phys. B* **45**, 085205 (2012).
- [23] E. Ghanbari-Adivi, *J. Phys. B* **44**, 165204 (2011).
- [24] E. Ghanbari-Adivi and H. Ghavaminia, *Phys. Scr.* **89**, 105402 (2014).
- [25] S. Ghosh, A. Dhara, C. R. Mandal, and M. Purkait, *Phys. Rev. A* **78**, 042708 (2008).
- [26] R. Samanta, M. Purkait, and C. R. Mandal, *Phys. Rev. A* **83**, 032706 (2011).
- [27] P. N. Abufager, P. D. Fainstein, A. E. Martínez, and R. D. Rivarola, *J. Phys. B* **38**, 11 (2005).
- [28] U. Chowdhury, A. L. Harris, J. L. Peacher, and D. H. Madison, *J. Phys. B* **45**, 035203 (2012).
- [29] M. Zapukhlyak, T. Kirchner, A. Hasan, B. Tooke, and M. Schulz, *Phys. Rev. A* **77**, 012720 (2008).
- [30] S. Houamer, Y. V. Popov, and C. Dal Cappello, *Phys. Rev. A* **81**, 032703 (2010).
- [31] Dž. Belkić, *Phys. Rev. A* **47**, 3824 (1993).
- [32] Dž. Belkić, *J. Phys. B* **10**, 3491 (1977).
- [33] I. M. Cheshire, *Proc. Phys. Soc.* **84**, 89 (1964).
- [34] D. Dollard, *J. Math. Phys.* **5**, 729 (1964).
- [35] I. Mančev, N. Milojević, and Dž. Belkić, *Phys. Rev. A* **86**, 022704 (2012).
- [36] I. Mančev, N. Milojević, and Dž. Belkić, *Phys. Rev. A* **88**, 052706 (2013).
- [37] Dž. Belkić, R. Gayet, J. Hanssen, I. Mančev, and A. Nuñez, *Phys. Rev. A* **56**, 3675 (1997).
- [38] C. J. Joachain and R. Vanderpoorten, *Physica* **46**, 333 (1970).
- [39] G. W. F. Drake, M. M. Cassar, and R. A. Nistor, *Phys. Rev. A* **65**, 054501 (2002).
- [40] Dž. Belkić, *J. Phys. B: At. Mol. Opt. Phys.* **30**, 1731 (1997).
- [41] Dž. Belkić, *Nucl. Instrum. Methods Phys. Res. B* **124**, 365 (1997).
- [42] E. Hylleraas, *Z. Phys.* **54**, 347 (1929).
- [43] C. Eckart, *Phys. Rev.* **36**, 878 (1930).
- [44] J. N. Silverman, O. Platas, and F. A. Matsen, *J. Chem. Phys.* **32**, 1402 (1960).
- [45] L. Green, M. Mulder, M. Lewis, and J. W. Woll, *Phys. Rev.* **93**, 757 (1954).
- [46] P. Löwdin, *Phys. Rev.* **90**, 120 (1953).
- [47] F. W. Byron and C. J. Joachain, *Phys. Rev.* **146**, 1 (1966).
- [48] S. C. Mukherjee, K. Roy, and N. C. Sil, *Phys. Rev. A* **12**, 1719 (1975).
- [49] Dž. Belkić, *Phys. Rev. A* **37**, 55 (1988).
- [50] J. R. Oppenheimer, *Phys. Rev.* **31**, 349 (1928).
- [51] Dž. Belkić, S. Saini, and H. S. Taylor, *Phys. Rev. A* **36**, 1601 (1987).
- [52] M. B. Shah, P. McCallion, and H. B. Gilbody, *J. Phys. B* **22**, 3037 (1989).
- [53] U. Schryber, *Helv. Phys. Acta* **40**, 1023 (1967).
- [54] M. B. Shah and H. B. Gilbody, *J. Phys. B* **18**, 899 (1985).
- [55] K. H. Berkner, S. N. Kaplan, G. A. Paulikas, and R. V. Pyle, *Phys. Rev.* **140**, A729 (1965).
- [56] J. F. Williams, *Phys. Rev.* **157**, 97 (1967).
- [57] L. M. Welsh, K. H. Berkner, S. N. Kaplan, and R. V. Pyle, *Phys. Rev.* **158**, 85 (1967).
- [58] P. J. Martin, K. Arnett, D. M. Blankenship, T. J. Kvale, J. L. Peacher, E. Redd, V. C. Sutcliffe, J. T. Park, C. D. Lin, and J. H. McGuire, *Phys. Rev. A* **23**, 2858 (1981).
- [59] P. Loftager (private communication).
- [60] E. Horsdal-Pedersen, C. L. Cocke, and M. Stockli, *Phys. Rev. Lett.* **50**, 1910 (1983).
- [61] Dž. Belkić, S. Saini, and H. S. Taylor, *Z. Phys. D* **3**, 59 (1986).
- [62] R. P. Feynman, *Phys. Rev.* **76**, 769 (1949).
- [63] Dž. Belkić, *J. Phys. B* **26**, 497 (1993).
- [64] Dž. Belkić and H. S. Taylor, *Phys. Rev. A* **35**, 1991 (1987).
- [65] M. R. C. McDowell and J. P. Coleman, *Introduction to the Theory of Ion-Atom Collisions* (North-Holland, Amsterdam, 1970).
- [66] M. Abramowitz and I. A. Stegun, *Handbook of Mathematical Functions with Formulas, Graphs, and Mathematical Tables* (Dover, New York, 1972).